



**HAL**  
open science

# Analyse de la qualité image et inter-étalonnage des radars à ouverture synthétique aéroportés du JPL (USA) et du DLR (RFA)

P. Olivier

## ► To cite this version:

P. Olivier. Analyse de la qualité image et inter-étalonnage des radars à ouverture synthétique aéroportés du JPL (USA) et du DLR (RFA). [Rapport de recherche] Note technique - CRPE n° 189, Centre de recherches en physique de l'environnement terrestre et planétaire (CRPE). 1990, 58 p., illustrations, tableaux, graphiques. hal-02191390

**HAL Id: hal-02191390**

**<https://hal-lara.archives-ouvertes.fr/hal-02191390>**

Submitted on 23 Jul 2019

**HAL** is a multi-disciplinary open access archive for the deposit and dissemination of scientific research documents, whether they are published or not. The documents may come from teaching and research institutions in France or abroad, or from public or private research centers.

L'archive ouverte pluridisciplinaire **HAL**, est destinée au dépôt et à la diffusion de documents scientifiques de niveau recherche, publiés ou non, émanant des établissements d'enseignement et de recherche français ou étrangers, des laboratoires publics ou privés.

RP 10396

**CENTRE NATIONAL D'ETUDES  
DES TELECOMMUNICATIONS**

**CENTRE NATIONAL DE LA  
RECHERCHE SCIENTIFIQUE**

**CENTRE DE  
RECHERCHES  
EN PHYSIQUE DE  
L'ENVIRONNEMENT  
TERRESTRE  
ET PLANETAIRE**

**CRPE**

**NOTE TECHNIQUE**

**CRPE/189**

**ANALYSE DE LA QUALITE IMAGE ET  
INTER-ETALONNAGE DES RADARS  
A OUVERTURE SYNTHETIQUE AEROPORTES  
DU JPL (USA) ET DU DLR (RFA)**

**Par**

**P. OLIVIER**

**INSTITUT DE L'INFORMATION  
SCIENTIFIQUE ET TECHNIQUE  
2, Allée du Parc de Brahois - Tél. 83.50.46.00  
INIST - 54514 VANDŒUVRE LÈS NANCY CEDEX**

**RPE/OBT  
38-40, rue du Général Leclerc  
92131 ISSY-LES-MOULINEAUX, FRANCE**

G 76038

CENTRE NATIONAL D'ETUDES  
DES TELECOMMUNICATIONS  
Centre Paris B

CENTRE NATIONAL DE LA  
RECHERCHE SCIENTIFIQUE  
Département TOAE

**CENTRE DE RECHERCHES EN PHYSIQUE DE  
L'ENVIRONNEMENT TERRESTRE ET PLANETAIRE**

NOTE TECHNIQUE CRPE/189

**ANALYSE DE LA QUALITE IMAGE ET  
INTER-ETALONNAGE DES RADARS  
A OUVERTURE SYNTHETIQUE AEROPORTES  
DU JPL (USA) ET DU DLR (RFA)**

par

**P. OLIVIER  
RPE/OBT**

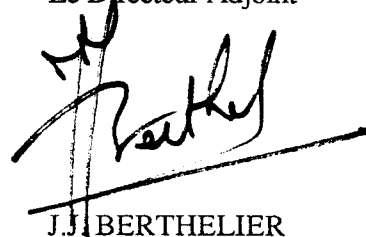
38-40 rue du Général Leclerc  
92131 ISSY-LES-MOULINEAUX

Le Directeur



G. SOMMERIA

Le Directeur Adjoint



J.J. BERTHELIER

Octobre 1990

LISTE DE DIFFUSION SYSTEMATIQUE

CNET

MM. FENEYROL                    Directeur du CNET  
 THABARD                        Directeur Adjoint  
                                      du CNET  
 COLONNA                        Adjoint Militaire  
                                      au Directeur du CNET  
 MEREUR                         Directeur  
                                      des Programmes  
 BLOCH                          DICET  
 THUE                             DICET  
 MME HENAFF                    DICET

MM. PIGNAL                    **PAB**  
 RAMAT                          PAB  
 NOBLANC                       PAB-BAG  
 ABOUDARHAM                  PAB-SHM  
 HOCQUET                       PAB-STC  
 THEBAULT                      PAB-STG  
 SOMMERIA                      PAB-RPE  
 GENDRIN                       PAB-RPE  
 BAUDIN                         PAB-RPE  
 BERTHELIER                   PAB-RPE  
 BIC                              PAB-RPE  
 CERISIER                       PAB-RPE  
 LAVERGNAT                     PAB-RPE  
 ROBERT                         PAB-RPE  
 ROUX                            PAB-RPE  
 TESTUD                        PAB-RPE  
 VIDAL-MADJAR                PAB-RPE  
 MME HAUSER                   PAB-RPE

CNRS

MM. BERROIR                    TOAE  
 CHARPENTIER                  SPI  
 MME SAHAL                     TOAE  
 MM. COUTURIER                INSU  
 MME LEFEVRE                  DR  
 M. DUVAL                       DR

CNES

MMES AMMAR  
 DEBOUZY  
 MM. BAUDOIN  
 FELLOUS  
 HERNANDEZ (Toulouse)

Bibliothèques

CNET-SDI (3)  
 CNET-EDB  
 CNET-RPE (Issy) (5)  
 CNET-RPE (St Maur) (2)  
 Observatoire de Meudon  
 CNRS-SA  
 CNRS-CDST  
 CNRS-LPCE

LISTE COMPLEMENTAIRE

LAA/ELR/DNP  
 PAB/BAG/CMM  
 PAB/SHM/PHZ  
 PAB/RPE  
 PAB/RPE/OBT  
 PAB/RPE/OBT  
 PAB/RPE/OBT  
 PAB/RPE/OPN  
 PAB/RPE/ITS

VAUTIER  
 CAQUOT  
 JUY  
 GENDRIN  
 CAUDAL  
 DECHAMBRE  
 HAUSER  
 TACONET  
 LE QUEAU  
 LANCELIN

CCETT - RENNES

DOCUMENTATION

CNES

CNES/OT                        BAUDOIN

EXTERIEUR

GSTS  
 DMN/EERM  
 TRT

BECKER  
 LOITIERE  
 MARTIN

## RESUME

Ce document constitue le compte-rendu technique de la mission effectuée par l'auteur, de Février à Juillet 1990, au sein du Jet Propulsion Laboratory (USA). Le travail a consisté en une étude comparative, du point de vue de la qualité image et de l'étalonnage, d'images obtenues, sur le site d'Oberpfaffenhofen (RFA), par deux Radars à Ouverture Synthétique aéroportés aux caractéristiques sensiblement différentes.

L'analyse de la qualité image a permis de mettre en évidence les propriétés spécifiques des deux systèmes, polarimétrie complète du ROS de NASA/JPL et haute résolution multi-vues du ROS du DLR, et d'attester que les objectifs de qualité respectifs étaient, dans l'ensemble, atteints.

Les images en bande C ont été séparément étalonnées, polarimétriquement par l'utilisation d'un algorithme développé au JPL et radiométriquement au moyen de coins réflecteurs triédraux disposés à cet effet sur la scène imagée. La comparaison effectuée ensuite sur les coefficients de rétro-diffusion de cibles étendues a fourni des résultats encourageants puisque les valeurs obtenues diffèrent de moins de 2 dB.

Enfin, et ceci constitue l'aspect le plus original de ce travail, on a montré qu'un inter-étalonnage effectif était faisable entre les deux séries de données, notamment en ce qui concerne la correction radiométrique en site des images ROS.

## REMERCIEMENTS

Le travail décrit dans le présent document a été effectué, au cours d'un séjour de cinq mois, au Jet Propulsion Laboratory, California Institute of Technology, sur un contrat de la National Aeronautics and Space Administration. Le financement du séjour a été assuré par le Centre National d'Etudes des Télécommunications et par le Centre National des Etudes Spatiales. Que le Dr. D. Vidal-Madjar, responsable du département Observation de la Terre, soit particulièrement remercié pour avoir pris l'initiative d'une telle collaboration.

L'auteur est reconnaissant envers les Drs. F. Li, J. Curlander et R. Kwok de l'avoir accueilli respectivement dans leur section et groupe, A. Freeman d'avoir fourni le sujet de l'étude et de l'avoir fait progresser par de nombreuses et fructueuses discussions, et tous les membres de l'équipe "étalonnage" (particulièrement P. Dubois, J. Holt et J. Klein) pour la mise à disposition de tout matériel ou logiciel nécessaire ainsi que leur assistance humaine quasi journalière. Les équipes respectives des ROS aéroportés de NASA/JPL et du DLR doivent aussi être remerciées pour avoir recueilli et traité les données utilisées dans ce travail.

## CONTENTS

- 1. Introduction**
- 2. Description of the experiment**
  - 2.1 The JPL multi-frequency, multi-polarization Aircraft SAR
  - 2.2 The DLR C-Band and X-Band E-SAR
  - 2.3 The DLR, Oberpfaffenhofen, experimental site
- 3. Image quality analysis**
  - 3.1 Radiometric resolution
  - 3.2 Spatial resolution
    - 3.21 AIRSAR C-Band images
    - 3.22 E-SAR C-Band and X-Band images
- 4. Amplitude calibration of the E-SAR C-Band image**
  - 4.1 Model for amplitude calibration
  - 4.2 Actual calibration
  - 4.3 E-SAR calibration for distributed targets
- 5. Polarimetric calibration of the AIRSAR C-Band images**
  - 5.1 Model for polarimetric calibration
  - 5.2 Actual calibration
- 6. Cross-calibration of E-SAR and AIRSAR images**
- 7. Conclusion**

## REFERENCES

## TABLES

## FIGURES

## 1. Introduction

In summer 1989, the NASA/JPL DC-8 SAR took part in a series of calibration experiments in Europe: three different sites were imaged in the UK (Feltwell), NL (Flevoland) and FRG (Oberpfaffenhofen), and several sensors (including SAR and SLAR) were in operation. The aims of this campaign were multiple: to check the calibration performance of the JPL Aircraft SAR (named AIRSAR in the following) over European sites, of quite different texture compared with those previously used in North America; to compare, from the image quality and calibration points of view, the images provided by the different sensors; to test various equipment and approaches for ground calibration and to help find candidate sites for future satellite missions such as SIR-C and ERS-1.

A detailed description and some preliminary results of these multi-sensor experiments can be found in [1]. In this document, we will deal only with data gathered from the German site over which both AIRSAR and the German E-SAR, the latter on board a Dornier DO228, flew along parallel tracks, on the same day of August 1989. Having at our disposal the whole fully polarimetric three frequency (L-, C- and P-Band) data set from the AIRSAR and the C- and X-Band, VV polarized, amplitude images from the E-SAR, the purpose of this work was to conduct a comparative image analysis and calibration of these two data sets. The main features of such a study should be: to point out the specific characteristics of each data set, considering the very different radars which were in operation (better spatial resolution for the E-SAR, quad-polarization mode of the AIRSAR...); and to be able to perform effective cross-calibration, i. e. use one calibrated image to improve the calibration process of the other one.

Thus, the plan of this study follows, logically:



- Check the image quality of the two data sets, using standard tools like radiometric resolution, impulse response parameters.

- Perform separate calibration of each image using a subset of the deployed devices on the airfield; for polarimetric calibration of the AIRSAR data, some algorithms developed at the JPL will be used.

- Compare the calibrated images by checking the target responses in areas away from the one used during the calibration process. Improve the E-SAR calibration process (particularly the range radiometric variation), since the present standard product of this system does not include all the necessary corrections, by means of the AIRSAR image, which is considered to be fairly well calibrated because of the previously conducted calibration experiments, mainly Goldstone in Spring 1988 [2],[3].

- Finally, original conclusions should be drawn about the usefulness of such cross-calibration analysis; for it is the first time, as far as we know, that SAR imagery of the same site is performed by two different radars, under similar conditions.

But let us first give a brief description of the two radar imaging systems and of the experimental site at Oberpfaffenhofen.

## 2. Description of the experiment

### 2.1 The JPL multi-frequency, multi-polarization Aircraft SAR

The principal parameters of the NASA/JPL Airborne Imaging Radar [4] are gathered on Table 1: as an experimental tool for preparing the future SIR-C mission, this system was designed to be multi-frequency (P-, L- and C-Band), fully polarimetric (i. e. providing complex data in each of the four polarization channels HH, HV, VH, VV). The important characteristics to keep in mind are that basically the same chirp signal is used, for the three frequencies, and that the transmitted pulse is alternatively switched on H and V polarizations within the same pulse repetition interval.

The twelve simultaneously acquired coherent channels are processed using SAR standard frequency domain compression algorithms, with Hamming weighting function being applied in range and in azimuth, in order to reduce sidelobes (this point is important to be noted for it will have a direct consequence on the image quality parameters such as spatial resolution and sidelobe levels).

Among the three available standard products, high resolution single look complex image, compressed four-look Stokes matrix format or survey mode image, only the first one was used here. The high resolution format includes twelve separated files, corresponding to each frequency/polarization channel, containing 750 records of 4096 azimuth pixels; the sampling steps are 6.7 m in slant range and 3.0 m in azimuth.

## 2.2 The DLR C-Band and X-Band E-SAR

The E-SAR system allows imagery in three frequencies, L-, C- and X-Band, with only VV polarization [5]. Since only C- and X-Band data were obtained over the Oberpfaffenhofen site, we report on Table 1 and 2 the radar parameters related to these two frequencies. The important characteristics which differ from the JPL radar are the followings (regarding C-Band) :

- The platform flies at rather low altitudes, which implies a larger aperture beamwidth in elevation to illuminate a given swath

- The theoretical range spatial resolution is smaller than the AIRSAR one, while both SAR azimuth spatial resolutions are of the same order of magnitude.

The raw data are range compressed on board the aircraft, by means of a Surface Acoustic Wave correlator, and the signal is radiometrically controlled by an AGC/STC unit, placed at the pulse compression module input, in order to fit the system dynamic range. A motion compensation procedure is incorporated, prior to the on-ground azimuth compression, which extracts the desired parameters from the range compressed data [6].

The data products we have at our disposal are multi-look (4-look C-Band and 8-look X-Band) amplitude detected images in slant range coordinates.

## 2.3 The DLR, Oberpfaffenhofen, experimental site

The DLR site, located near Munich in Germany, is centered on the airport area, where the calibration devices were deployed, and contains various background areas as grasslands, forests, agricultural fields and suburban areas. As shown on Figure 1, a set of 55 pieces of calibration equipment were installed, mainly in the airfield area, including various sized trihedrals (from 0.4 m to 1.0

m) and dihedrals (0.7 m and 1.0 m), one C-Band receiver unit and one C-Band Polarimetric Active Radar Calibrator. The dihedrals were oriented at  $0^\circ$  and  $45^\circ$ , with respect to the line of sight direction, by means of a DLR built, very precise pointing system in azimuth, elevation and orientation. Most of the trihedrals were deployed as single ones, but some of them were gathered in pairs, separated by about 10 m, in order to test the resolution capabilities of the sensors.

On two consecutive days of August 1989, both radars, mounted on board their respective platforms, flew several parallel flights oriented at  $42^\circ$  (parallel to the runway direction) and  $132^\circ$  (orthogonal to the runway) with respect to North, with various incidence angles for the AIRSAR radar (about  $20^\circ$ ,  $35^\circ$  and  $50^\circ$  over the airfield main runway).

In Figures 2, 3 and 4 are respectively displayed the CVV AIRSAR, CVV and XVV E-SAR images of the test site; all of them are amplitude detected. The E-SAR images are not radiometrically corrected; they are direct outputs from the SAR processor. Although we could perform the range radiometric correction, by means of vertical antenna pattern data and incidence angle knowledge, we preferred to keep these raw images, in order to conduct the cross-calibration analysis with the AIRSAR images. On each image, we can clearly see the airfield area with the corner reflector array; the calibration devices which are deployed near the buildings, below the runway, are not so clearly visible on these prints, with the exception of the PARC on C-Band pictures, but are more detectable on the imaging device screen. Scales and aspects of these three images are variable to each other because of the different values taken by the resolution and the pixel spacing parameters. Table 2 summarizes the image parameters, from the three data sets we will deal with in the following sections, i. e. C-Band quad-polarization AIRSAR, C-Band and X-Band VV polarized E-SAR, all along the  $42^\circ$  direction flight path.

### 3. Image quality analysis

To assess the quality of one given SAR image, we usually deal with two main concepts: the radiometric resolution, which is a measurement of the ability of distinguishing two uniform areas of different backscattering coefficients, and spatial resolution, which is a measurement of the ability to separate two distinct point target scatterers. Image quality assessment is a very important step in SAR image study because the aim of a SAR is to provide ground reflectivity images with a much better spatial resolution (in azimuth) than a classical radar; so, it is obviously necessary to check to what extent this goal has been achieved. Moreover, for calibration purposes, with the aim of providing relationships between measured pixel intensities and ground reflectivity parameters, the radiometric resolution is a useful tool to estimate the accuracy of the obtained calibration results.

As such analysis is to be performed within each image and deals mainly with magnitude pixel responses, all the polarimetric quality checks, which can be made on the AIRSAR data set, will be treated in section 5, as part of the polarimetric calibration process.

#### 3.1 Radiometric resolution

On SAR images, the response of uniform (also called distributed) targets is disturbed by the well known speckle noise [7], due to the coherent addition of numerous and independent target responses within a same resolution cell. The power of this multiplicative noise directly affects the separability of two different areas, as it widens each probability density function of the pixel intensities; so a standard parameter to quantify the radiometric resolution is provided by the  $\sigma/\mu$  ratio, where  $\mu$  and  $\sigma$  are the mean and standard deviation of the pixel intensity

distribution over selected uniform areas.  $\sigma$  and  $\mu$  represent respectively the multiplicative noise and desired signal powers, so this radiometric resolution parameter can be seen, too, as a signal to speckle noise ratio.

A common way of expressing the radiometric resolution coefficient allows a direct interpretation in dB:

$$\gamma = 10 \log ( 1 + \sigma/\mu ) \quad (1)$$

where  $\sigma$  and  $\mu$  are computed from the power (not amplitude) pixel distribution [8].

Assuming the elementary scatterer responses, within one cell, are complex, independent random variables with the same probability distribution, it can be shown that the power of the resulting signal is exponentially distributed while its phase is uniformly distributed over  $[0; 2\pi]$ . So the radiometric resolution coefficient should be 1 (3.01 in dB) when estimated from power detected single-look uniform areas.

Considering multi-look images, which result from the superposition of  $N$  independent power detected partial images, the mean and standard deviation of the pixel intensity probability density are respectively multiplied by  $N$  and  $\sqrt{N}$ , so that the radiometric resolution coefficient becomes:

$$\gamma_N = 10 \log \left( 1 + \frac{1}{\sqrt{N}} \right) \quad (2)$$

Thus, in order to assess the image radiometric quality, we selected a set of ten uniform areas (by visual inspection) in each of the three images (only CVV was considered in the AIRSAR case) and then computed the associated  $\gamma$

coefficient. The average results are reported on Table 3, as well as the expected values, from (2), knowing that the AIRSAR data are 1-look (since they are, actually, complex images) and the E-SAR data are respectively 4 (C-Band) and 8 (X-Band) look images.

Measured and expected values for the AIRSAR CVV image are in good agreement, but, concerning the E-SAR, measured values are higher than expected (the difference is more important for the X-Band image). This discrepancy can be explained by the fact that the four, or eight, looks are not perfectly independent to each other, hence a less efficient speckle noise reduction: during the multi-look processing, the selected Doppler sub-bands, instead of being completely disjointed, exhibited a certain amount (50%) of overlap. However, a 50% bandwidth overlap, inducing respectively 2.5 and 4.5 equivalent number of independent looks, should lead to even higher values of the  $\gamma$  coefficient.

### 3.2 Spatial resolution

Spatial resolution properties of a SAR image are most conveniently studied by means of the whole system impulse response (including the measurement radar equipment and the image synthesis signal processor), i. e. the response provided by an isolated point target scatterer located on an (almost) perfectly absorbing background. Such point targets are the corner reflector devices deployed on the calibration area; they are preferred to natural targets which are likely to be less adequately located and of poorer "point-like" characteristics.

From the two-dimensional impulse response, the following parameters can be extracted to characterize the image spatial quality:

- the spatial resolution itself, defined as the 3 dB (half power) width of the main lobe (in the range and azimuth directions)

- the Peak Sidelobe Ratio, measured by the level of the highest sidelobe relatively to the main lobe level, which is relevant to the possible existence of artifacts in the vicinity of the target

- the Integrated Sidelobe Ratio, measured by the total power lying in the sidelobes relatively to the main lobe power, which indicates the power amount which is dispersed outside the target actual location and could corrupt other scatterer responses.

These three sets of parameters are directly measurable from the images, containing many artificial point-like scatterers; summary tables of their values as well as typical plots of the impulse response will be provided in the following sub-sections.

### 3.21 AIRSAR C-Band images

On Figure 5 are plotted the impulse response magnitude of the  $45^\circ$  PARC, for the four polarization channels; this is the calibration target for which the sidelobes are the most apparent, since it has the best signal to noise (background) ratio (35 dB for like-polarization and 43 dB for cross-polarization). The four responses are pretty similar, as they must be, because of the theoretical  $45^\circ$  PARC scattering matrix (see (17d)).

Azimuth cuts of the HH and VH polarization impulse responses are plotted on Figure 6, where we can remark that the first sidelobes are only about 17 dB below the main lobe level, which is not as good a PSLR ratio as it should be expected from the weighting function applied during the SAR processing. For visual comparison purposes, range cuts of  $45^\circ$  PARC and typical trihedral impulse responses are plotted on Figure 7: we note that the PARC response exhibits an



improvement on the sidelobe energy (better ISLR) but not on sidelobe maximum peak level.

Considering azimuthal corner reflector impulse responses, some trihedrals exhibit the double peak feature shown on Figure 8-a, associated with a poor general response behaviour. This tendency was reported previously, during the Goldstone calibration experiment in 1988 [3], and it was thought there was some problem due to the lack of motion compensation algorithm within the SAR processor, so that the data could be processed with a badly estimated drift angle. Of course, in such cases, the definition of main and side lobes should be taken with caution, and hence the 3 dB widths and sidelobe levels should not be very significant.

A summary of the impulse response parameters is given in Table 4: the measured values are statistical means and standard deviations among the thirteen 0.9 m trihedrals (taking into account both co-polarization channels) and averages over the 45° PARC four channels. The expected values were estimated during pre-flight system analysis and simulations; these calculations did not take into account the weighting functions which were actually introduced in the processor. So, the measured values are somewhat different from the predicted ones: greater 3 dB widths and better PSLR (the expected effects of a weighting function). The poor measured azimuth PSLR value from the trihedrals is to be related to the double-peak feature reported above. Anyway, the trihedral measured values are on the whole fairly close to the ones obtained during the Goldstone experiment [3], at least the mean values since there are some discrepancies among the standard deviations, which means a good long term stability of the AIRSAR performance. The PARC results are better than the trihedral ones as expected from the impulse response plots.

### 3.22 E-SAR C-Band and X-Band images

The same kind of quality checking plots are shown, for the E-SAR system, on Figures 9, C-Band 45° PARC impulse response, 10 and 11, C-Band and X-Band typical 0.9 m trihedral response. The first thing we can notice, this is particularly clear on the PARC signature, is the discrepancy in the range and azimuth sidelobe patterns: it is much higher in the range direction. This is, probably, due to the on board range processing of the raw data, by means of an analog SAW correlator, which is a less efficient method than numerical ones. Secondly, the PARC impulse response is much improved, regarding the sidelobe levels, with respect to the trihedral one; this is particularly true in the azimuth direction. Such an improvement was not so obvious in the AIRSAR case. This feature is the result of the multi-look processing which flattens the sidelobe pattern and makes it reach the background level (see the range and azimuth cuts of Figure 11); so the higher PARC signal to background ratio leads directly to a better PSLR coefficient.

On Table 5 are reported the measured impulse response parameters from the thirteen 0.9 m trihedrals and from the C-Band PARC. The estimated resolutions are pretty close to the predicted ones (see Table 2), except for the X-Band 3 dB width in azimuth, where the 4.0 m expected value maybe is under-estimated regarding the 8-look process which was applied.

When comparing with C-Band results of Table 4, the difference between the numerical values of the PSLR and ISLR parameters confirm the sidelobe pattern reduction brought by the multi-look processing. This is true as well for the azimuth direction, where both system space resolutions are of the same order of magnitude, as for the range direction, where E-SAR spatial resolution is much smaller. Only the range ISLR improvement is less important, for the above mentioned reason of analog range processing of the data.

Finally, the main feature of this comparison analysis is the much lower variability of the impulse response parameters over the C-Band trihedral data, as pointed out by the standard deviation low values.

So, one of the most interesting conclusions we can draw from this comparative quality analysis is that the SAR multi-look processing, while primarily designed in order to increase the image radiometric resolution by reducing the speckle noise power, also improves the impulse response quite well. We must note that these good spatial resolution properties of the multi-look image imply that there was no offset problems between the individual images (or they were well corrected), prior to their superposition.

#### 4. Amplitude calibration of the E-SAR C-Band image

##### 4.1 Model for amplitude calibration

The assumptions we will make, in order to establish the relationship between the pixel intensities of one SAR image and the terrain backscattering parameters, are the followings: first, point target, clutter area and noise responses are three different processes which are statistically independent to each other, so that the received signals add in power to form the measured pixel intensity; secondly, the best estimate of point target cross-section is provided by the integrated pixel power over a sufficiently large area containing most of the scatterer impulse response energy, as was recommended by [9].

Thus, the radar equation, giving the measured integrated power  $P_r$  over an area  $A$  surrounding one given point target scatterer, can be formulated as [10]:

$$P_r = H \frac{P_t G^2 \lambda^2 \sigma}{(4\pi)^3 R^4} + P_n \quad (3)$$

where

- $\sigma$  ( $= \sigma_t + A \sigma^0$ ) is the total cross-section (clutter+target) of the area  $A$ .
- $P_t$  is the transmitted power
- $G$  is the antenna gain, in the target direction
- $\lambda$  is the radar wavelength
- $R$  is the slant range
- $H$  is the SAR gain, including the processing gain
- $P_n$  is the noise power, integrated over  $A$ .

We can re-write (3), separating each contribution, as:

$$P_r = C K(R) \sigma_t + C K(R) \sigma^0 A + P_n \quad (4)$$

with  $C = \frac{P_t \lambda^2}{(4\pi)^3}$  is a constant term and  $K(R) = \frac{H G^2}{R^4}$  is the range (or incidence angle) dependent factor.

Let us apply the previous formula to three different areas within a local part of the image (where the noise and clutter properties are constant):

.  $A_3$  where there is only noise:

$$P_3 = P_n = P_{n0} A_3 \quad (5)$$

where  $P_{n0}$  is the noise power density

.  $A_2$  where there is clutter and noise:

$$P_2 = (C K(R) \sigma^0 + P_{n0}) A_2 \quad (6)$$

.  $A_1$  where the studied point target scatterer lies, which response is mixed with the noise and clutter area:

$$P_1 = C K(R) \sigma_t + (C K(R) \sigma^0 + P_{n0}) A_1 \quad (7)$$

From (6) and (7), we can derive the calibration factor expression, as a function of the measured  $P_1$  and  $P_2$ :

$$C K(R) = \frac{P_1 - P_2 A_1 / A_2}{\sigma_t} \quad (8)$$

and, then, from (5) and (6), we obtain an estimate of the distributed target backscattering coefficient:

$$\sigma^0 = \frac{P_2 / A_2 - P_3 / A_3}{C K(R)} \quad (9)$$

once the calibration factor is determined.

The R dependence, in the previous relationships, only means that all the integrated power calculations should be performed over areas of same slant range;

consequently, the obtained calibration factor should be valuable only over a small slant range interval.

#### 4.2 Actual calibration

The same set of thirteen 0.9 m trihedrals (see Figure 1) was used to perform amplitude calibration of both E-SAR and AIRSAR images: they constitute the only set of identical corner reflectors in sufficient number to allow reasonable RCS estimation by computation of their average responses; moreover, they lie on a ground area of limited size, thus avoiding the effects of the range radiometric variation shown by the E-SAR images.

A summary of these trihedral responses is given in Figure 12, where the integrated power, minus background power, is plotted in dB versus the scatterer location in range, Figure 12-a, and in azimuth, 12-b, for both frequency bands. The integrated power minus background power is an estimate of the numerator of (8), apart from a multiplicative constant (additive in dB) which is the pixel size ( $1.5 \times 1.5 \text{ m}^2$  in slant range).

By examination of the C-Band plots, it can be stated that there is no significant variation among the corner reflector responses, neither in range nor in azimuth, except for a fade affecting three trihedrals located within a common range line. This fade is to be related to a general attenuation which affects several contiguous range lines of the C-Band image, as it can be observed from a thorough examination of this image radiometry. So, this is an artifact, the cause of which is not exactly known (maybe an inaccurately estimated azimuthal

reference function during the SAR processing), and these three corner reflectors should be removed for further studies.

Considering the X-Band plots, the corner reflector responses exhibit large fluctuations, with a standard deviation of 1.9 dB, and a general level increase with range location; these variations can be explained by the location of the calibration area, near the image top edge, where the antenna pattern fall-off effect is too much important. So, no reasonable calibration procedure of this image could be attempted with such features; thus, in the following of this E-SAR calibration section, we will only deal with the C-Band data set.

Since the ten selected corner reflectors are identical 0.9 m trihedrals and are close enough to each other to produce no range response variation, an estimate  $S_1$  of the integrated power minus background associated with this kind of scatterer is provided by the calculated average over these targets:

$$S_1 = 75.6 \text{ dB with s. d.} = 0.2 \text{ dB}$$

The theoretical radar cross-section of a triangular trihedral of maximum length  $a$ , at frequency  $f$ , is [11]:

$$RCS_{\text{tri}} = \frac{4\pi a^4 f^2}{3 c^2} \quad (10)$$

The E-SAR C-Band frequency is 5.3 GHz and  $a = 0.9$  m, so  $RCS_{\text{tri}} = 29.3$  dB and the calibration correction factor for point target cross-section estimation is

$$-C K(R) \text{ (dB)} = RCS_{\text{tri}} - S_1 = -46.3 \text{ dB}$$

### 4.3 E-SAR calibration for distributed targets

From equation (9), it appears that the calibrated value of the backscattering coefficient of any given distributed target is provided by the difference between the mean pixel power density and the noise power density, divided by the calibration factor  $C K(R)$ . These mean power densities should be calculated over large enough areas, in order to greatly reduce the speckle contribution in the uniform area response. As the previously given value of  $S_1$  in reality the total pixel power within the integration area (i. e. the integrated power divided by the pixel area), the calibration factor to get the backscattering coefficient is

$$\begin{aligned} & - C K(R) \text{ (dB)} - A_g \text{ (dB)} \quad \text{or} \\ & - C K(R) \text{ (dB)} - A_s \text{ (dB)} + 10 \log (\sin \theta) \end{aligned} \quad (11)$$

where  $A_g$  and  $A_s$  are respectively the ground and slant pixel size, and  $\theta$  is the incidence angle.

In the area where the trihedrals were deployed,  $\theta = 40^\circ$  and the pixel sizes are 1.5 m in slant range and azimuth for C-Band data. So the calibration correction factor for distributed target backscattering coefficient determination is -51.7 dB.



## 5. Polarimetric calibration of the AIRSAR C-Band images

### 5.1 Model for polarimetric calibration

The aim of a fully polarimetric SAR is to provide measurements of the target scattering matrix:

$$S = \begin{pmatrix} S_{hh} & S_{vh} \\ S_{hv} & S_{vv} \end{pmatrix} \quad (12)$$

The  $S_{ij}$  complex element of  $S$  is the target response when one  $i$ -polarized wave is transmitted and the measurement is made on the  $j$ -polarized receiver; here  $i$  and  $j$  represent one of the orthogonal horizontal and vertical polarizations. Since any given polarization state can be written as a linear combination of these two former ones, we can derive, from the  $S$  knowledge, the target response corresponding to arbitrary transmit and receive polarizations [12].

Assuming a linear model to describe the transmitter and receiver perturbations, the observed scattering matrix  $O$  can be written, as a function of the desired one  $S$ :

$$O = \begin{pmatrix} O_{hh} & O_{vh} \\ O_{hv} & O_{vv} \end{pmatrix} = \begin{pmatrix} R_{hh} & R_{hv} \\ R_{vh} & R_{vv} \end{pmatrix} \begin{pmatrix} S_{hh} & S_{vh} \\ S_{hv} & S_{vv} \end{pmatrix} \begin{pmatrix} T_{hh} & T_{vh} \\ T_{hv} & T_{vv} \end{pmatrix} + \begin{pmatrix} N_{hh} & N_{vh} \\ N_{hv} & N_{vv} \end{pmatrix} \quad (13)$$

where  $N = \{N_{ij}\}$  is an additive noise matrix and  $R = \{R_{ij}\}$  and  $T = \{T_{ij}\}$  are the receive and transmit matrices:  $T_{ij}$  (resp.  $R_{ij}$ ) is the transmit (receive)  $j$ -channel response to  $i$ -polarized incident radiation; in (13), the transposed notation in the receiving matrix only means that the receiver is seen as a transmitter acting in the reverse sense.

Ignoring the noise matrix  $N$  in (13), if we want to retrieve the desired scattering matrix  $S$  from the observed  $O$ , we have to determine the  $T$  and  $R$  perturbation matrices (this is the purpose of polarimetric calibration). The transmitter and receiver matrices can be split into three terms in order to separate different effects:

$$T = \begin{pmatrix} T_{hh} & T_{vh} \\ T_{hv} & T_{vv} \end{pmatrix} = T_{hh} \begin{pmatrix} 1 & T_{vh}/T_{vv} \\ T_{hv}/T_{hh} & 1 \end{pmatrix} \begin{pmatrix} 1 & 0 \\ 0 & T_{vv}/T_{hh} \end{pmatrix} \quad (14)$$

and

$$R = \begin{pmatrix} R_{hh} & R_{vh} \\ R_{hv} & R_{vv} \end{pmatrix} = R_{vv} \begin{pmatrix} 1 & R_{vh}/R_{vv} \\ R_{hv}/R_{hh} & 1 \end{pmatrix} \begin{pmatrix} R_{hh}/R_{vv} & 0 \\ 0 & 1 \end{pmatrix} \quad (15)$$

So the observed matrix can be re-written as:

$$O = T_{hh} R_{vv} \begin{pmatrix} R_{hh}/R_{vv} & 0 \\ 0 & 1 \end{pmatrix} \begin{pmatrix} 1 & R_{hv}/R_{hh} \\ R_{vh}/R_{vv} & 1 \end{pmatrix} S \begin{pmatrix} 1 & T_{vh}/T_{vv} \\ T_{hv}/T_{hh} & 1 \end{pmatrix} \begin{pmatrix} 1 & 0 \\ 0 & T_{vv}/T_{hh} \end{pmatrix} + N \quad (16)$$

where the following terms have been isolated:  $R_{hv}/R_{vv}$ ,  $R_{vh}/R_{vv}$ ,  $T_{hv}/T_{hh}$  and  $T_{vh}/T_{vv}$  terms produce cross-polarization contamination (so called "cross-talk" terms);  $R_{hh}/R_{vv}$  and  $T_{vv}/T_{hh}$  are the channel imbalance terms between the two orthogonal polarizations; and  $T_{hh} \cdot R_{vv}$  is the absolute calibration factor.

Several algorithms [13] [14] [15] have been developed to provide estimates of these calibration parameters from a given polarimetric image: generally, they use various combinations of known point targets (Polarimetric Active Radar Calibrators, trihedrals, dihedrals,...), located in the imaged scene, the number and configuration of which depending upon the assumptions made on the backscattering  $S$  and system  $T$  and  $R$  matrices. The calibration technique we have

used in the present study [16] avoids the drawback of needing numerous man-made corner reflectors and is based upon a minimum set of hypothesis: the backscattering statistics of natural distributed targets within the image are used to remove the cross-talk contamination, only assuming the scatterers are reciprocal (i. e.  $S_{vh} = S_{hv}$ ) and the like- and cross-polarized channels are uncorrelated, which is theoretically assessed in the case of azimuthally symmetric natural targets [17]; known corner reflectors, as trihedrals, can then be used to eliminate the channel amplitude/phase imbalance and to absolute calibrate the data. The principal steps of this algorithm are given in the following:

- cross-talk removal: compute the covariance matrix of S from distributed targets in the area of interest, assuming some kind of spatial ergodicity; solve equations derived from (16), using both previously mentioned assumptions, in the cross-talk parameter unknowns  $R_{hv}/R_{vv}$ ,  $R_{vh}/R_{vv}$ ,  $T_{hv}/T_{hh}$  and  $T_{vh}/T_{vv}$ ; this resolution involves some iterative process in order to estimate the correlation coefficients of the cross-polarization scattering terms  $S_{hv}$  and  $S_{vh}$

- channel imbalance removal: the availability of a trihedral corner reflector in the studied scene allows determination of the  $R_{hh}/R_{vv}$  and  $T_{vv}/T_{hh}$  terms, since the HH and VV responses of a trihedral are known to be identical

- absolute calibration: knowledge of the trihedral cross-section leads straightforwardly to the absolute calibration factor amplitude  $|T_{hh} \cdot R_{vv}|$ . The best way to estimate the measured cross-section of a point target scatterer, from the data set, was adressed in the previous section dedicated to amplitude calibration.

It is to be noted that the whole algorithm assumes that the unknown T and R matrices are constant; so it must be applied only to small areas (in the range direction) and repeted as many times as necessary, in order to correct an entire image.

## 5.2 Actual calibration

The algorithm we have just described above has been applied to the AIRSAR C-Band data to provide polarimetric calibrated images. The first part of this algorithm, i. e. the covariance matrix computations and cross-talk parameter estimation, was performed using the first quarter of the images (most left-sided on Figure 2), since it was the one which contained the greatest percentage of uniform areas and which was farthest away from most of the point target scatterers (calibration devices on the airport and urban point-like reflectors). Then the cross-talk removal procedure was applied to the whole image with the previously estimated parameters. The channel imbalance was removed by means of the average measured response from the thirteen 0.9 m trihedrals:

$$\text{HH/VV mean amplitude} = 0.2 \text{ dB with s. d.} = 0.7 \text{ dB}$$

$$\text{HH/VV mean phase} = 145.4^\circ \text{ with s. d.} = 3.8^\circ$$

Finally, absolute calibration was obtained via the known trihedral RCS in order to get backscattering coefficient ( $\sigma^0$ ) calibrated data files. From the thirteen 0.9 m trihedrals, the mean measured amplitude response was:

$$\text{HH} = 34.5 \text{ dB with s. d.} = 0.7 \text{ dB}$$

$$\text{VV} = 34.3 \text{ dB with s. d.} = 0.3 \text{ dB}$$

So, when comparing with the theoretical RCS of 29.3 dB, and taking into account the pixel size (13.0 dB) to get  $\sigma^0$  valued data, we obtained an absolute calibration correction factor of -18.0 dB, which was applied to the whole data.

Before we analyse the results of the calibration process, it is worth recalling the scattering matrices of the various target types used in the present experiment:

$$S_{\text{trihedral}} = \begin{pmatrix} 1 & 0 \\ 0 & 1 \end{pmatrix} \quad (17a)$$

$$S_{0^\circ \text{dihedral}} = \begin{pmatrix} 1 & 0 \\ 0 & -1 \end{pmatrix} \quad (17b)$$

$$S_{45^\circ \text{dihedral}} = \begin{pmatrix} 0 & 1 \\ 1 & 0 \end{pmatrix} \quad (17c)$$

$$S_{45^\circ \text{PARC}} = \begin{pmatrix} 1 & 1 \\ -1 & -1 \end{pmatrix} \quad (17d)$$

Results of the polarimetric calibration analysis, performed on the uncalibrated C-Band data and on the calibrated ones, are gathered on Table 6. HH/VV ratio is a measurement of the co-polarization channel imbalance, in amplitude and phase; same kind of information about the cross-polarized channels is provided by the HV/VH ratio, when estimated from rotated devices like 45° dihedrals. Cross-talk contamination estimation is given by the HV/HH and VH/HH amplitude ratios, from trihedrals (unsensitive to orientation), 0° dihedral (line of sight orientation) and 45° dihedral.

From examination of these results, we can make the following main comments:

- The uncalibrated data are already well balanced in amplitude, as well for the co-polarized channels as for the cross-polarized ones; thus, the calibration process did not improve so much the channel balance, except, obviously, for the trihedrals, of which the mean HH/VV complex ratio was actually used to perform the channel imbalance removal procedure.

- On the contrary, the raw data are not at all phase calibrated, for the HH/VV and HV/VH phases are quite different from the expected ones. The phase balance was achieved on the calibrated data, since the phase values are close to the 0° or 180° expected ones, within the allowable error margin.

- Cross-talk isolation levels are not high enough in the uncalibrated data, being at least 3 dB below the desired threshold of 30 dB; these levels reach acceptable values in trihedral and 45° dihedral calibrated data, while the improvement is very small in the case of the 0° dihedral. For corner reflectors

which are sensitive to orientation, such as the  $0^\circ$  dihedral, maybe that kind of bad cross-talk level can be explained by a non-perfect alignment of the corner reflector respectively to the line of sight direction, as was suggested in [1].

- The increase of the trihedral cross-talk level standard deviations, from uncalibrated to calibrated data, does not necessarily mean that the results are less reliable in the latter case; it can be explained by the fact that, with reduced cross-polarization contamination, the cross-polarized channel responses sometimes can be about or under the background level, thus giving rise to more variable numerical results. Anyway, the essential result is preserved, that is to say these responses lie under the desired cross-talk level.

To conclude this section, and to sum up the previous developments, we can assess the polarimetric calibration of the C-Band AIRSAR data has been achieved quite well.

## 6. Cross-calibration of E-SAR and AIRSAR images

Having performed absolute calibration of the two sensor C-Band images of the same site, by means of one set of identical trihedrals, we would like to compare the calibrated responses associated with other targets. As the ultimate goal of calibrating a SAR image is to provide physical values of the terrain backscattering coefficient, we will focus our attention on the distributed target responses provided by both images. Although the AIRSAR data set is fully polarimetrically calibrated, we will consider, in the following, only the VV-polarized magnitude image.

To compare the calibrated data of both radars, the first chosen approach is a global one: the mean pixel power, computed over several lines, is taken as an estimate of the average terrain backscattering coefficient; then, this mean pixel power is displayed as a function of the other direction, for relative calibration analysis purpose. Of course, the accuracy of such an estimate will be greatly degraded in areas where there are numerous point target scatterers, giving rise to spiky features on the curves. There is no problem when averaging whole azimuth lines, since there is no noticeable distortion of the pixel magnitude in this direction (except for a few range lines in the C-Band E-SAR image). However, when averaging range lines, we have to select previously a restricted interval around the main trihedral set (about 2 km wide), because of the E-SAR image global range variation.

These average backscattering coefficient curves are plotted on Figure 13, azimuth variation of range averaged power on 13-a and range variation of azimuth averaged power on 13-b. For easier comparison between the two data sets, on Figure 13-b the mean power is plotted versus ground position, referred to a common origin (one of the 0.9 m trihedrals). The selected intervals are identical

for both images, in each direction, and the average pixel power is computed over ten consecutive lines. The E-SAR curves exhibit more pronounced high frequency fluctuations, because of the smaller sampling steps, and resolutions, of this system; we can observe, too, on Figure 13-b, that the sampling steps are varying along the curves, due to the slant range to ground range conversion.

On Figure 13-a, the AIRSAR and E-SAR curves are very close to each other; even many spiky features are very similar, despite their point-like scatterer origin. Particularly remarkable is the curve fit at the right-end part of the plot where the areas are more likely to be uniform; here the curve difference absolute value is always less than 1 dB.

From the E-SAR plot on Figure 13-b, we can easily notice the following features: the global power variation with range is due to the lack of post-processor range correction (propagation loss, vertical antenna pattern); and the strong peak at the near range end is the nadir return, since the selected range window, in the SAR processor, included distances smaller than the minimal physical one (i. e. the aircraft altitude). But the most interesting result is the fact that both curves are pretty similar, in an absolute sense as well as in a relative one, over a ground range interval of more than 1 km length around the origin.

The AIRSAR image is well relatively calibrated (it is a confirmation) since the associated curve on Figure 13-b shows no noticeable global range variation. So this curve could be used as a reference in order to perform relative calibration of the E-SAR image across the range swath. But this is not a simple problem because the two curves do not have neither the same sampling frequency nor the same intrinsic resolution, so the calculation of the two function difference should not be so straightforward as it could appear at first sight. In the following, a rough attempt will be made to perform such relative cross-calibration and then to



compare with a standard theoretical range correction procedure. To do the latter, we first need to know the incidence angle variations with range, which will help, too, explain some discrepancies among the backscattering coefficient values provided by the two sensors. So, on Figure 14, curves of incidence angle versus ground range location are displayed for the two sensors. On the whole, incidence angles are quite different, particularly for near range areas; but, for the calibration area we are mainly interested in, around the origin, the difference is only about  $5^\circ$  (about  $45^\circ$  for AIRSAR and  $40^\circ$  for E-SAR), which should not lead to significant differences of the backscattering coefficient [18], if we assume the airport area to be mainly composed of grasslands.

On Figure 15 is plotted, as the solid curve, the empirical correction factor computed as the difference (in dB) between AIRSAR and E-SAR mean backscattering coefficients, versus ground range; the E-SAR function has been previously smoothed to fit the same sampling step as the AIRSAR one. Only the slow variations of this curve are to be considered, since the sharp and quick fluctuations we can observe are due to unavoidable ground range misregistrations between the two initial functions. The dashed curve represents the theoretical calibration function, taking into account all the range (or incidence angle) effects: vertical antenna pattern, propagation loss and incidence angle correction for backscattering coefficient calculation. From equation (11) and the expression (4b) of the  $K(R)$  factor, we can derive the formula giving, in power, the calibration correction factor relative to the backscattering level at the ground origin:

$$CAL = \frac{\sin(\theta_0) R_0^4}{H(R_0) G(R_0)^2} \cdot \frac{H(R) G(R)^2}{\sin(\theta) R^4} \quad (18)$$

The processor gain  $H(R)$  is proportional to the squared slant range, as in most standard SAR processors. Thus, the previous expression finally becomes:

$$CAL = \frac{\sin(\theta_0) R_0^2}{G(R_0)^2} \cdot \frac{G(R)^2}{\sin(\theta) R^2} \quad (19)$$

as it is plotted on Figure 15. The theoretical curve seems actually to be a good fit of the empirical one, at least in an area of more than 2 km length around the origin. Of course, both functions are zero-valued at the ground origin, by the way they are built.

The good fit between these two curves indicates that the E-SAR image could have been range corrected only by means of an external image of the same site, from a sensor with rather different characteristics. As it is the first time two sensor images are radiometrically compared this way, this is a very encouraging result, all the more because of the rather preliminary state of the present cross-calibration study. In case of developing such kind of cross-calibration method, we should be able to define a more elaborate and cautious strategy, by solving the following problems: how to deal with different sensor sampling steps and resolutions? how to filter the spiky features due to point target reflectors? what is the best way to modelise the relative calibration function?...But this should be the subject of future works.

The second way of comparing the AIRSAR and E-SAR calibrated images is more natural and more precise, if performed cautiously!, than the previous one; but it is not much emphasized here because it necessitates many tedious human operations on the displayed images and thus cannot be developed in a systematic manner for further automatic analysis. Some uniform areas are visually selected

on each image, then the corresponding calibrated backscattering coefficient are evaluated, according to (9).

On Table 7 are gathered the comparative results of ten scenes of various terrain types: grasslands, fields and forests are commonly studied vegetation terrains; the airport runway and one urban area are added only for comparisons, as respectively representative of flat target and non-uniform distributed target extreme cases. For sake of completeness, HH channel results are provided from AIRSAR data. Also are given both system incidence angles and radiometric resolution coefficients (standard deviation to mean value ratio of the pixel power distribution) in order to check the area uniformity and to give some informations about scene texture, as seen by the two sensors.

The given backscattering coefficient values, in the E-SAR case, are corrected in range by the theoretical calibration function examined above. The obtained results are rather good, since the VV  $\sigma^0$  difference often lies about or within 1 dB and is never greater than 2.2 dB; but they are very much variable, in an uninterpretable way: there is no clear correlation of the result quality neither with the terrain type nor with the incidence angle difference. Obviously, the urban area result is not good since it is not a uniform target (see the great values taken by the  $\sigma/\mu$  coefficient). Another and more interesting discrepancies are exhibited by forest areas, as well from the backscattering coefficients as from the  $\sigma/\mu$  ratios: while the AIRSAR latter values are pretty close to 1, the expected value, the E-SAR ones are quite far away from 0.5 (corresponding to four-look). Maybe this discrepancy can be explained by the different sensor resolutions, the E-SAR resolution being too small to be able to see forests as uniform areas; in that case, the scattering mechanism should have been created mainly by trunks and branches (which are less numerous in each cell size) rather than by leaves.

## 7. Conclusion

For the first time, a comparative study of two different airborne SAR images of a same site has been thoroughly undertaken: image quality analysis and external, ground target based, calibration have been performed, from the NASA/JPL aircraft SAR C-Band and DLR E-SAR C-Band and X-Band data collected over the Oberpfaffenhoffen airport test site in FRG.

On the whole, both system data sets met the image quality requirements associated to their respective characteristics; the only observed discrepancies between theoretical and measured quality parameters could be explained by mis-estimation of some parameters during pre-flight design goal calculations: weighting functions actually used in the AIRSAR processor were not fully taken into account; and evaluation of the equivalent number of independent looks, in the E-SAR image formation, should be more exactly conducted. The AIRSAR performance was found to be stable when comparing with the previous Goldstone calibration experiment[3]; even some azimuth impulse response degradation still remains to be solved, the cause is thought to be the lack of motion compensation algorithm in the processor. The use of a PARC, compared with trihedrals, for spatial resolution analysis, leads to better impulse response parameter measured values, due to its greater signal to background ratio; particularly, it allowed to point out a discrepancy between the range and azimuth sidelobe patterns, which seemed to be produced by the on board analog range compression scheme used to process the E-SAR raw data.

The comparative image quality study has shown that the multi-look processing, more than improving the radiometric resolution, as it is designed for, produced decreased side lobe levels(PSLR and ISLR), and thus improved spatial

resolution, and, what is maybe the most important, more stable and reliable impulse response parameters, over the trihedral set used in the study.

Separate calibration procedures of both system C-Band images have been performed, using the same 0.9 m trihedral set. The radiometric calibration process of the E-SAR image has been addressed in detail, particularly focussing on some aspects which must be treated with care, such as point target RCS estimation taking into account the noise and background response, range dependence of the derived calibration factors, and point target RCS vs clutter  $\sigma^0$  formulation. Fully polarimetric calibration has been performed on AIRSAR C-Band images, by means of clutter backscattering statistics [16]: cross-polarization contamination has been markedly reduced and phase channel balance has been achieved to a high degree of quality.

Comparison between distributed target backscattering coefficients, evaluated from the previously calibrated C-Band images, gave rather good results, in an absolute sense, since  $\sigma^0$  differences always were below 2 dB, but some variability, within each terrain type, was detected and remained unexplained. A noticeable result was that the different spatial resolutions led to some discrepancies in the image contrast (radiometric resolution coefficient) on such areas as forests.

Finally, we have shown that effective cross-calibration between the different sensor images was feasible: the radiometric calibration of the E-SAR C-Band image actually could be achieved only by reference to the corresponding AIRSAR image, which was assumed properly calibrated, giving quite similar correction curves as those obtained from more classical methods (i. e. range radiometric correction and absolute calibration by means of known corner reflectors).

Further works in such direction of calibrating SAR images should include the definition of a cautious strategy mainly in order to deal with sensors of very different characteristics (spatial resolution, geometric configuration,...), since present and future calibration campaigns may involve various kinds of sensors, such as SARs, SLARs or scatterometers.

## REFERENCES

- [1] Freeman, A., et al., Preliminary results of the multi-sensor, multi-polarization SAR calibration experiments in Europe 1989, Proc. IGARSS '90, Washington, U. S. A., May 1990.
- [2] Freeman, A., Werner, C. and Klein, J. D., Results of the 1988 NASA/JPL airborne SAR calibration campaign, Proc. IGARSS '89, Vancouver, Canada, July 1989, pp. 249-253.
- [3] Freeman, A., Calibration and image quality assessment of the NASA/JPL aircraft SAR during spring 1988, JPL document D-7197, Feb. 1990.
- [4] Held, D. N., et al., The NASA/JPL multifrequency, multipolarization airborne SAR system, Proc. IGARSS '88, Edinburgh, Scotland, Sept. 1988, pp. 345-350.
- [5] Horn, R., C-Band SAR results obtained by an experimental airborne SAR sensor, Proc. IGARSS '89, Vancouver, Canada, July 1989, Vol. 4, pp. 2213-2216.
- [6] Moreira, J., A new method of aircraft motion error extraction from radar raw data for real time SAR motion compensation, Proc. IGARSS '89, Vancouver, Canada, July 1989, Vol. 4, pp. 2217-2220.
- [7] Madsen, S. N., Speckle theory: modelling, analysis, and applications related to Synthetic Aperture Radar data, Electromagnetics Institute, LD 62, Technical University, Lyngby, Denmark, Nov. 1986.

- [8] Brown, L. M. J., et al., SAR data quality assessment and rectification, GEC-Marconi final report, ESA contract n° 6635/86/HGE-I, March 1988.
  
- [9] Gray, A. L., Vachon, P. W., Livingstone, C. E., and Lukowski, T. I., Synthetic aperture radar calibration using reference reflectors, IEEE Trans., GRS-28, n° 3, May 1990, pp.374-383.
  
- [10] Larson, R. W., Jackson, P. L., and Kasischke, E. S., A digital calibration method for synthetic aperture radar systems, IEEE Trans., GRS-26, n° 6, Nov. 1988, pp. 753-763.
  
- [11] Ruck, G. T., et al., Radar cross-section handbook, Plenum, New-York, 1970, Vol. 2, p.588.
  
- [12] Elachi, C., Spaceborne radar remote sensing: applications and techniques, IEEE Press, 1987.
  
- [13] Sheen, D. R., Freeman, A. and Kasischke, E. S., Phase calibration of polarimetric radar images, IEEE Trans., GRS-27, n° 6, Nov. 1989, pp. 719-731.
  
- [14] Freeman, A., Shen Y. and Werner, C. L., Polarimetric SAR calibration experiment using active radar calibrators, IEEE Trans., GRS-28, n° 2, March 1990, pp. 224-240.
  
- [15] van Zyl, J. J., Calibration of polarimetric radar images using only image parameters and trihedral corner reflector responses, IEEE Trans., GRS-28, n° 3, May 1990, pp. 337-348.



- [16] Klein, J. D., Calibration of complex quad-polarization SAR imagery using backscatter statistics, submitted to IEEE AES.
- [17] Borgeaud, M., Shin, R. T. and Kong, J. A., Theoretical models for polarimetric radar clutter, J. Electromagnetic Waves and Applications, Vol. 1, n° 1, 67-68, 1987.
- [18] Ulaby, F. T., and Craig Dobson, M., Handbook of radar scattering statistics for terrain, Artech House, 1989, p. 179.

Table 1. NASA/JPL AIR SAR and DLR E-SAR Parameter

Frequency Band	NASA/JPL AIR SAR			DLR E-SAR	
	P-Band	L-Band	C-Band	C-Band	X-Band
Center Frequency (MHz)	438.75	1298.75	5298.75	5300	9600
Pulse Length ( $\mu$ s)	11.25	11.25	11.25	5	5
Bandwidth (MHz)	19	19	19	100	100
El. 3 dB Beamwidth (dg)	38	44	50	35	30
Az. 3 dB Beamwidth (dg)	19	8	2.5	17	15
Pulse Rep. Frequency (Hz)		0.680 x V (knots)		952.38	1240
Mode			Quad. Pol.	VV	VV
Digital sampling rate (MHz)			45 (real)	100	100
No. of bits/sample			8	6 (I/Q)	6 (I/Q)
Processed Doppler Bandwidth (Hz)			70	75	110

Table 2. Parameters of the C-Band AIRSAR, C- and X-Band E-SAR Images Over DLR Site. Resolutions are Theoretical Ones, and Pixel Spacings are Values for the Images Displayed on Figs. 2, 3 and 4.

	AIRSAR C-BAND	E-SAR C-BAND	E-SAR X-BAND
Slant range resolution (m)	8.0	2.2	2.6
Azimuth resolution (m)	3.0	4.0	4.0
Range sampling step (m)	6.66	1.5	1.5
Azimuth sampling step (m)	3.03	1.5	0.93
Range pixel spacing (m)	6.66	3.0	3.0
Azimuth pixel spacing (m)	12.1	3.0	3.7
Range sample number	750	1700	2000
Azimuth sample number	4096	2048	4096

Table 3. Measured and Expected Radiometric Resolution Coefficients on Uniform Areas from Power Detected AIRSAR and E-SAR Images

	AIRSAR CVV	E-SAR CVV	XVV
Measured $\gamma_N$ (dB)	3.11	1.88	1.59
Expected $\gamma_N$ (dB)	3.01 (1-Look)	1.76 (4-Look)	1.31 (8-Look)

Table 4. Spatial Resolution Image Quality: Summary of Impulse Response Parameters for AIRSAR C-Band Data. Measured Values are Averages and Standard Deviations over 13 Trihedrals, HH and VV Polarizations, and Averages of 45° PARC Four Channels

	Design Goals	Measured	
		0.9 m Trihedrals	45° PARC
3 dB width range (m)	8.0	10.0 ( $\pm$ 0.9)	10.7
3 dB width azimuth (m)	3.0	4.7 ( $\pm$ 1.5)	3.4
PSLR range (dB)	-16.0	-18.2 ( $\pm$ 1.5)	-18.0
PSLR azimuth (dB)	-13.0	-12.5 ( $\pm$ 3.3)	-16.4
ISLR range (dB)	-13.0	-13.1 ( $\pm$ 1.8)	-17.3
ISLR azimuth (dB)	-8.0	-8.8 ( $\pm$ 2.4)	-11.2

Table 5. Spatial Resolution Image Quality: Summary of Impulse Response Parameters for E-SAR C-Band and X-Band Data, Estimated from thirteen 0.9 m trihedrals and from the 45° PARC for C-Band

	C-Band		X-Band
	0.9 m trihedrals	45° PARC	0.9 m trihedrals
3 dB width range (m)	2.44 ( $\pm$ 0.24)	2.62	2.74 ( $\pm$ 0.30)
3 dB width azimuth (m)	4.12 ( $\pm$ 0.15)	3.75	6.80 ( $\pm$ 2.02)
PSLR range (dB)	-23.7 ( $\pm$ 1.6)	-25.2	-20.6 ( $\pm$ 3.9)
PSLR azimuth (dB)	-27.3 ( $\pm$ 1.1)	-39.9	-24.0 ( $\pm$ 2.0)
ISLR range (dB)	-12.6 ( $\pm$ 1.7)	-14.2	-11.1 ( $\pm$ 1.6)
ISLR azimuth (dB)	-15.0 ( $\pm$ 0.6)	-14.9	-15.1 ( $\pm$ 2.2)

Table 6. AIRSAR C-Band Polarimetric Calibration Results from In-Scene Corner Reflectors

Parameter	Reflector	Measured Values		Expected Values
		Uncalibrated	Calibrated	
HH/VV Ampl. (dB)	trihedrals	0.19 ( $\pm 0.68$ )	-0.01 ( $\pm 0.69$ )	0.0 ( $\pm 0.4$ )
	45° PARC	0.10	-0.13	0.0 ( $\pm 0.4$ )
	0° dihedral	-0.06	-0.22	0.0 ( $\pm 0.4$ )
HH/VV Phase (dg)	trihedrals	145.38( $\pm 3.76$ )	-0.08 ( $\pm 3.76$ )	0.0 ( $\pm 10$ )
	45° PARC	-36.6	178.20	180 ( $\pm 10$ )
	0° dihedral	-37.75	177.12	180 ( $\pm 10$ )
HV/HH Ampl. (dB)	trihedrals	-26.94 ( $\pm 3.07$ )	-34.87 ( $\pm 5.51$ )	$\leq -30$
	0° dihedral	-18.39	-20.99	$\leq -30$
	45° dihedral	21.08	39.94	$\geq 30$
VH/HH Ampl. (dB)	trihedrals	-26.54 ( $\pm 2.78$ )	-33.27 ( $\pm 7.34$ )	$\leq -30$
	0° dihedral	-18.43	-21.99	$\leq -30$
	45° dihedral	21.29	39.70	$\geq 30$
HV/VH Ampl. (dB)	45° dihedral	-0.21	0.24	0.0 ( $\pm 0.4$ )
HV/VH Phase (dg)	45° dihedral	27.17	-2.15	0.0 ( $\pm 10$ )

Table 7. Radiometric comparison of C-Band AIRSAR and E-SAR distributed target responses, from calibrated images

Area	AIRSAR			E-SAR				
	HH $\sigma^0$ (dB)	$\sigma/\mu$	VV $\sigma^0$ (dB)	$\sigma/\mu$	incidence angle (dg)	VV $\sigma^0$ (dB)	$\sigma/\mu$	incidence angle (dg)
runway	-19.3	1.15	-17.7	0.95	46.2	-17.5	0.53	43.1
grass	-13.1	0.93	-13.8	0.98	46.7	-12.4	0.55	44.0
grass	-14.0	1.01	-15.7	0.92	43.6	-13.9	0.52	34.2
field	-5.2	1.00	-6.6	0.97	43.2	-6.2	0.51	32.9
field	-9.5	1.14	-12.2	0.95	44.8	-11.0	0.51	38.3
field	-9.7	1.02	-9.9	1.01	45.3	-8.3	0.52	39.9
forest	-8.9	1.01	-9.6	0.99	45.1	-10.4	0.70	39.5
forest	-8.7	0.97	-8.1	1.14	49.3	-5.9	0.78	50.1
forest	-7.5	1.03	-7.4	1.00	43.5	-9.1	0.66	35.0
urban	2.9	2.86	-1.2	2.22	48.1	-3.1	3.03	48.2

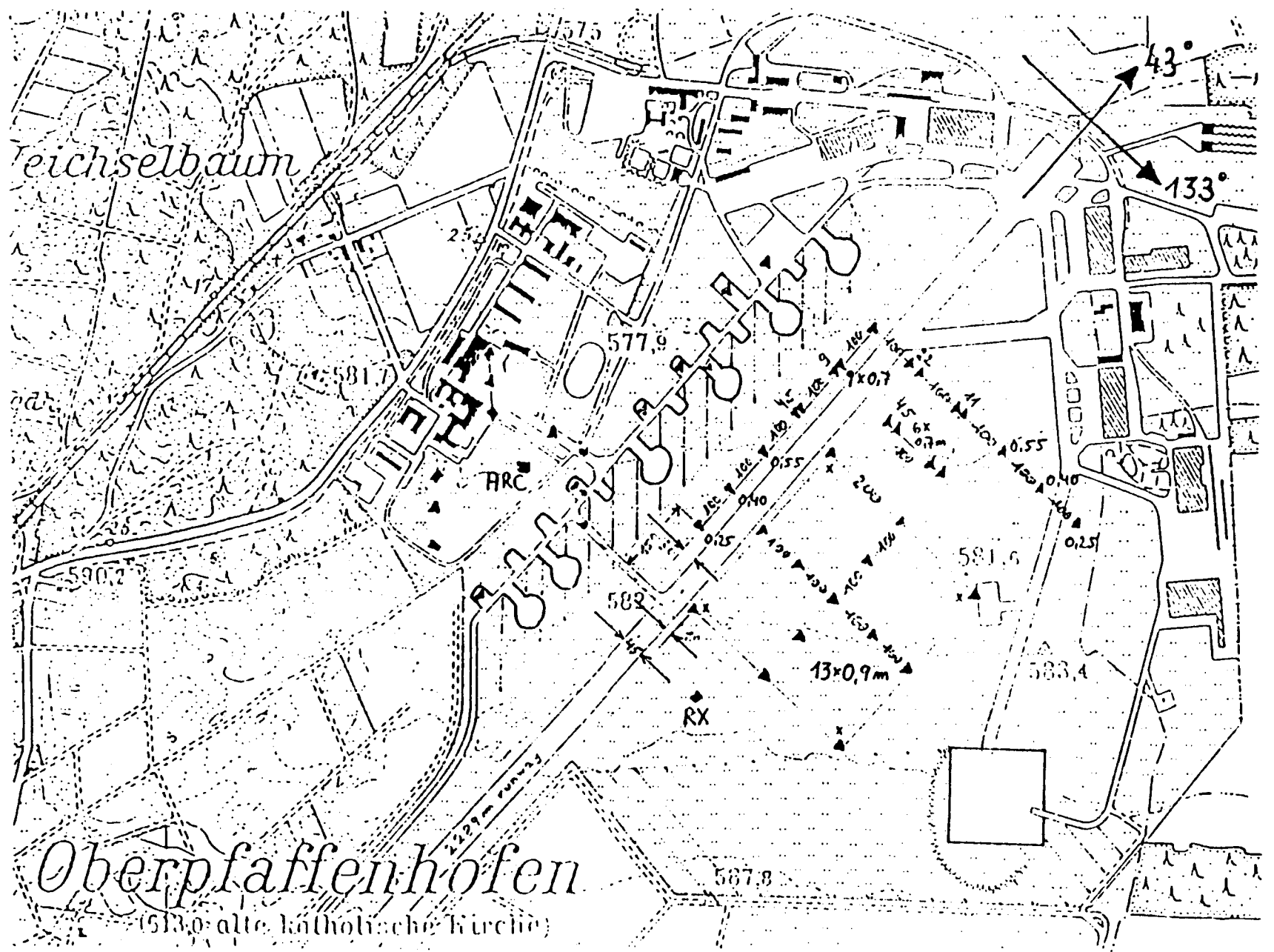


Figure 1. Map of the DLR calibration site at Oberpfaffenhofen



Figure 2. AIRSAR, C-Band VV polarization, amplitude image of the DLR test site



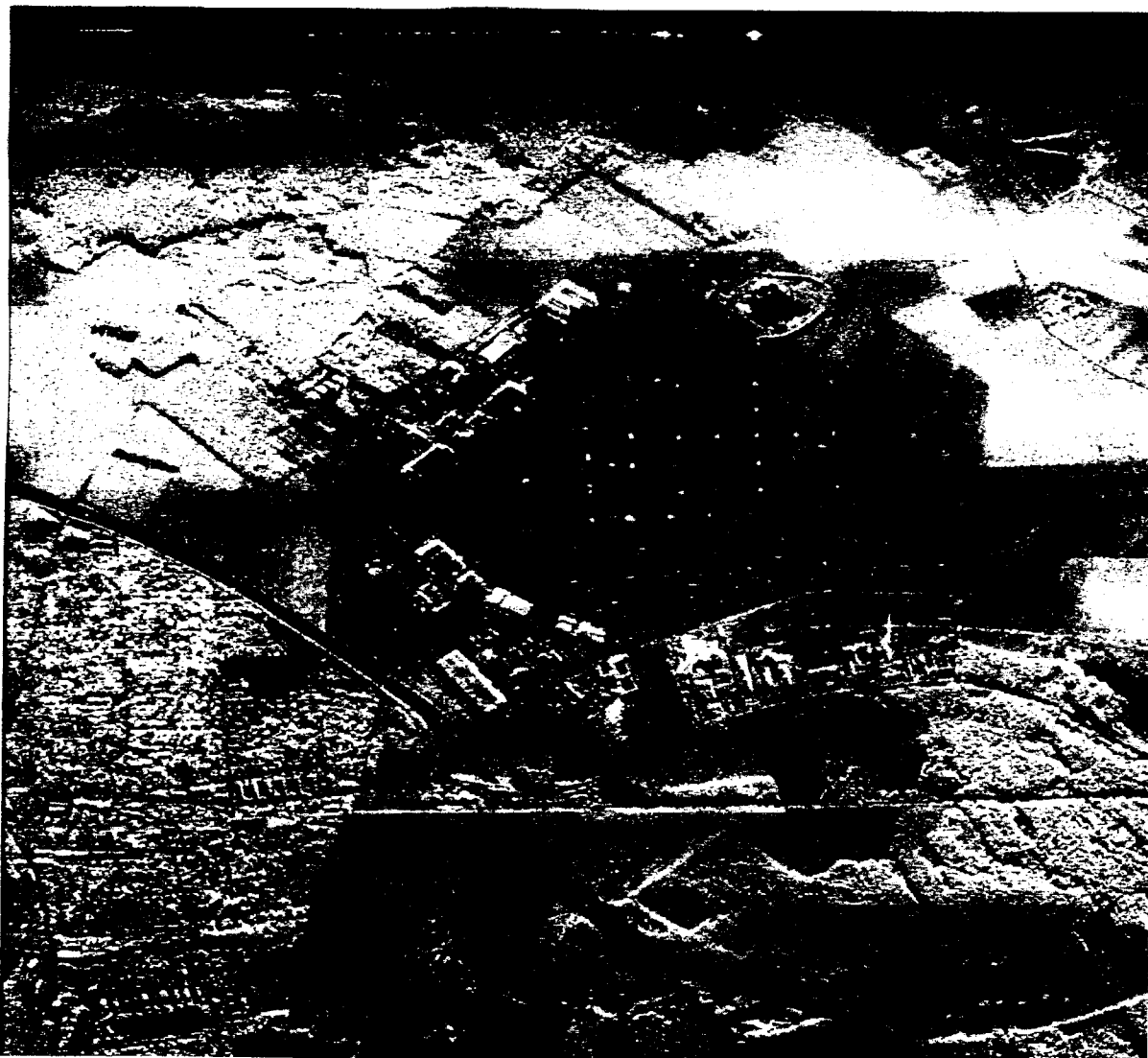


Figure 3. E-SAR, C-Band VV polarization, image of the DLR test site



Figure 4. E-SAR, X-Band VV polarization, image of the DLR test site

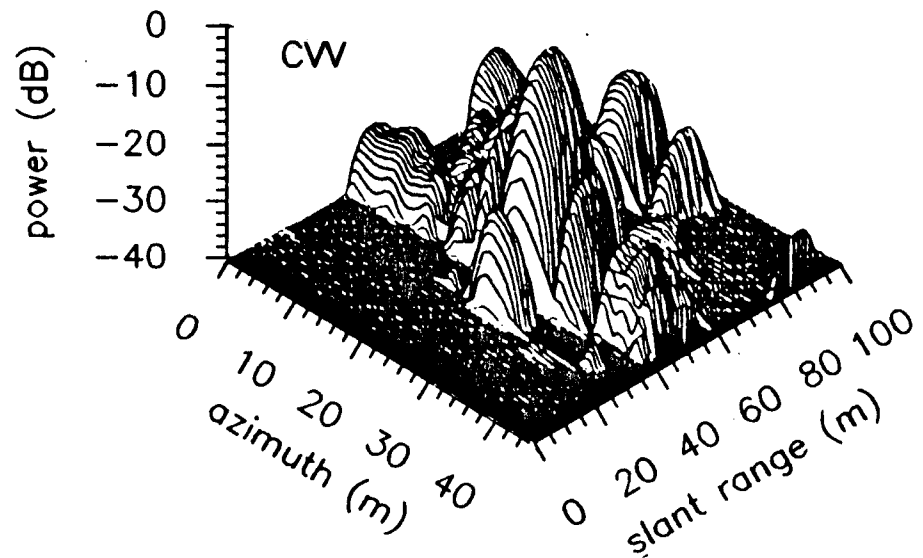
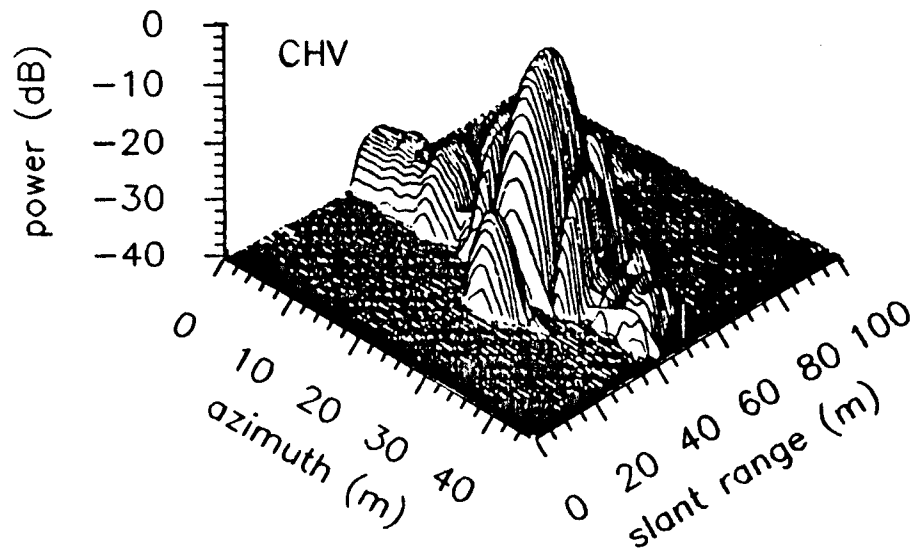
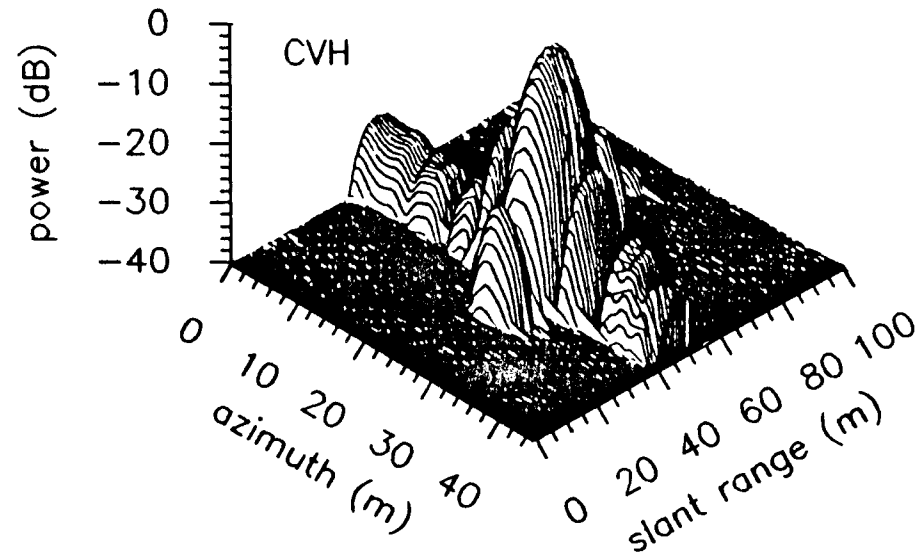
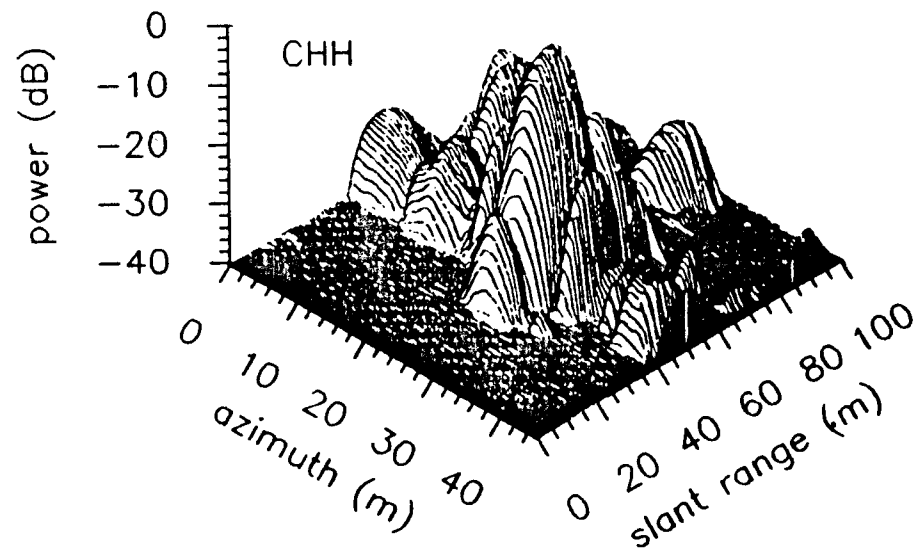


Figure 5. Impulse response of the 45° C-Band PARC, from AIRSAR quad-polarization data

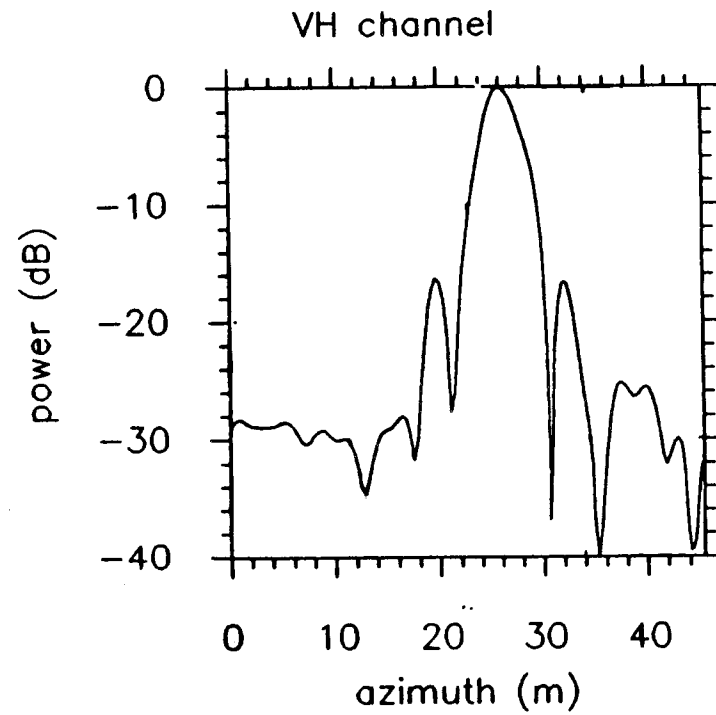
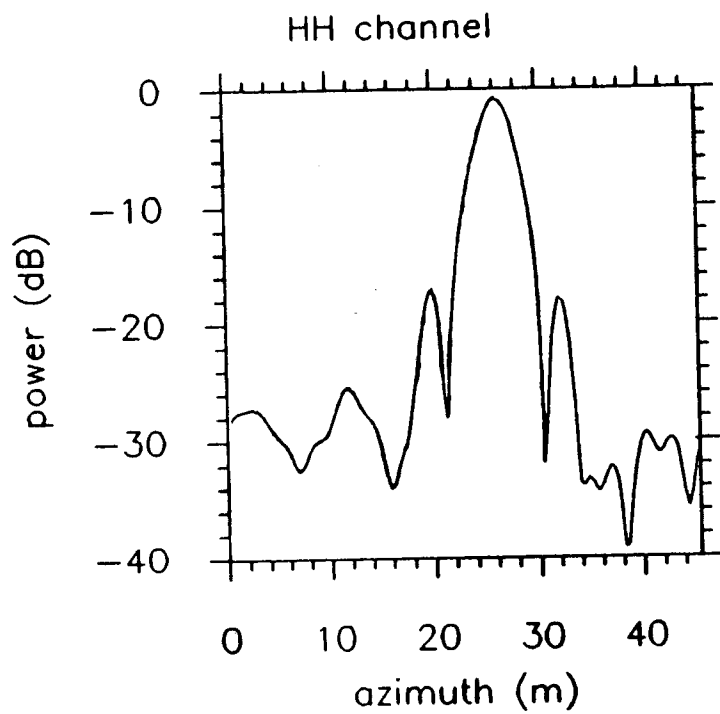


Figure 6. Azimuth cuts of the 45° PARC impulse response, from AIRSAR C-Band data, HH and VH channels (other channels are similar)

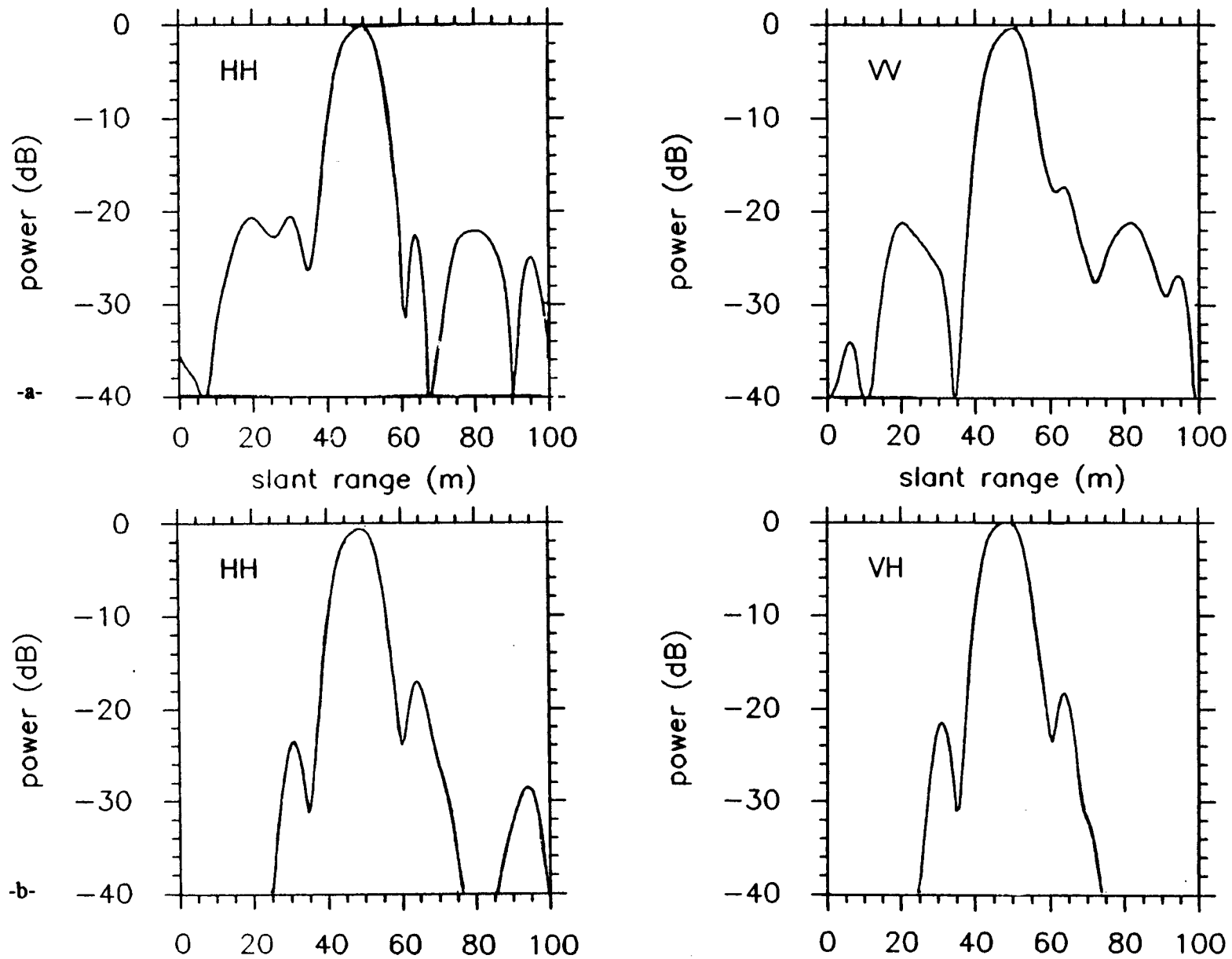


Figure 7. Range cuts of 0.9 m trihedral and 45° PARC impulse responses, from AIRSAR C-Band data; HH and VV channels for trihedral, HH and VH for PARC

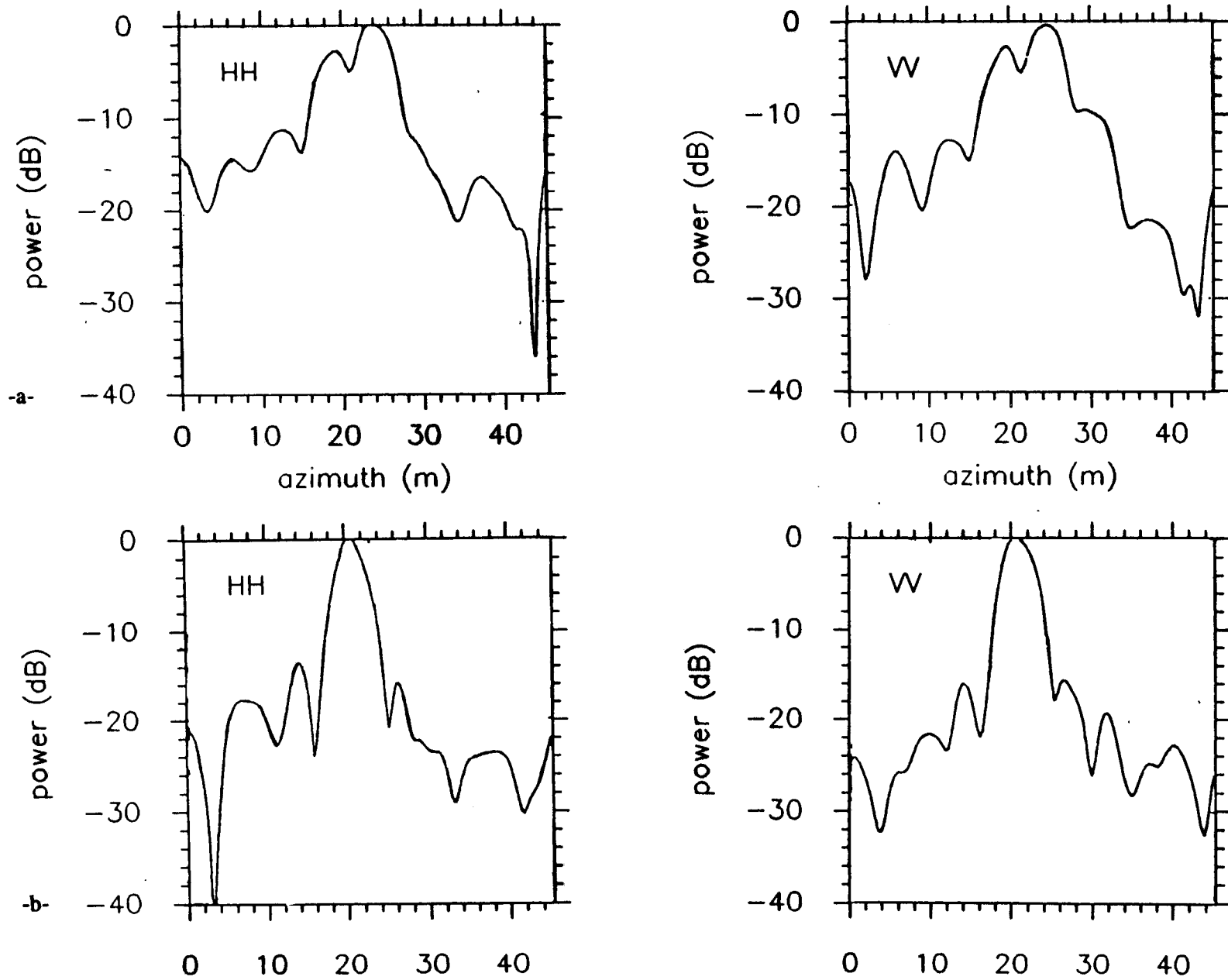


Figure 8. Worst case and best case 0.9 m trihedral azimuth impulse response from AIRSAR data, HH and VV channels

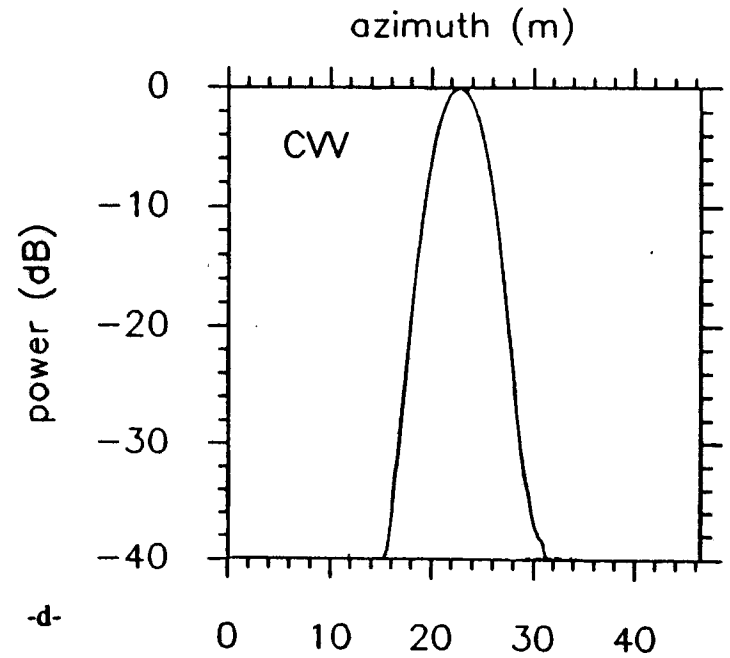
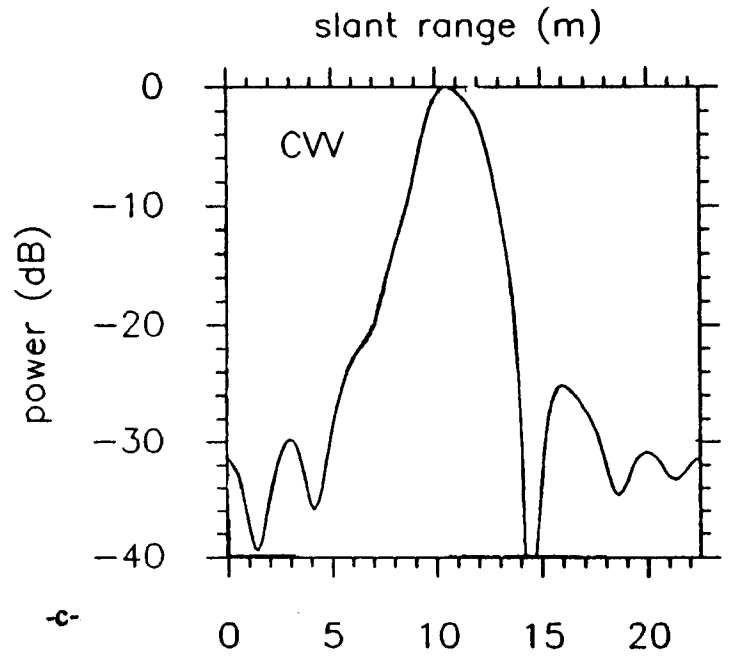
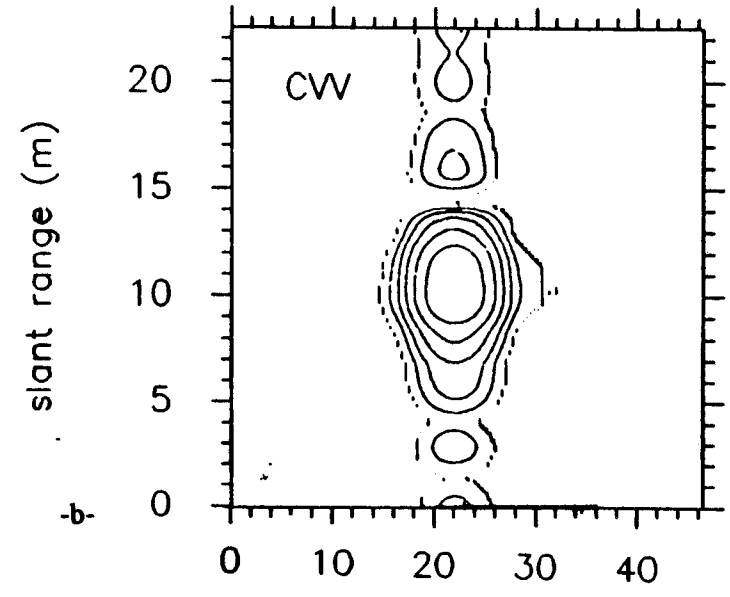
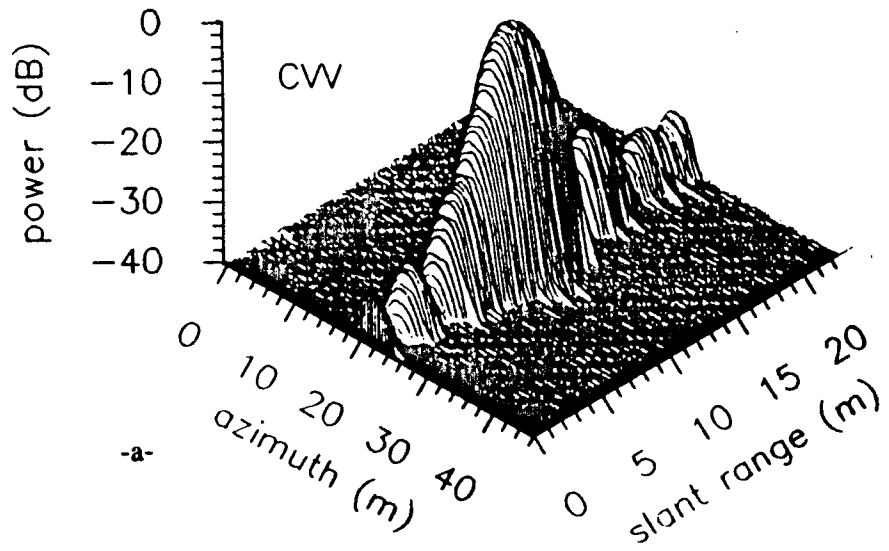


Figure 9. C-Band 45° PARC impulse response from VV polarized E-SAR data

a- 2-D impulse response      b- contour plot

c- range cut                      d- azimuth cut

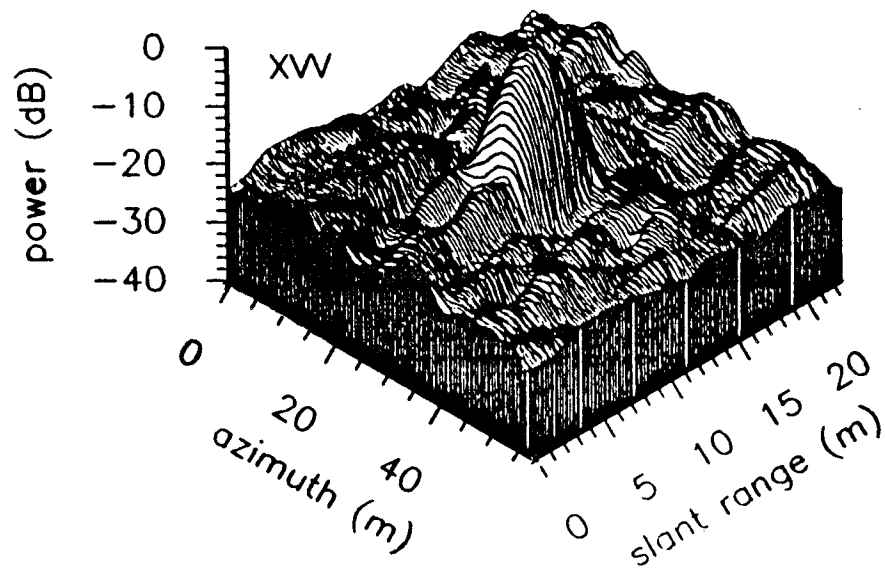
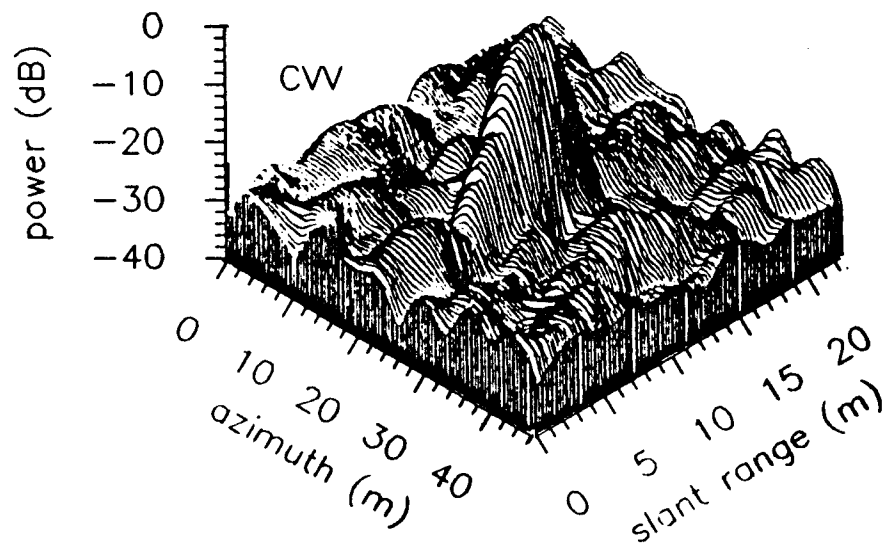


Figure 10. Two-dimensional impulse response of typical 0.9 m trihedral from E-SAR C-Band and X-Band VV polarized data



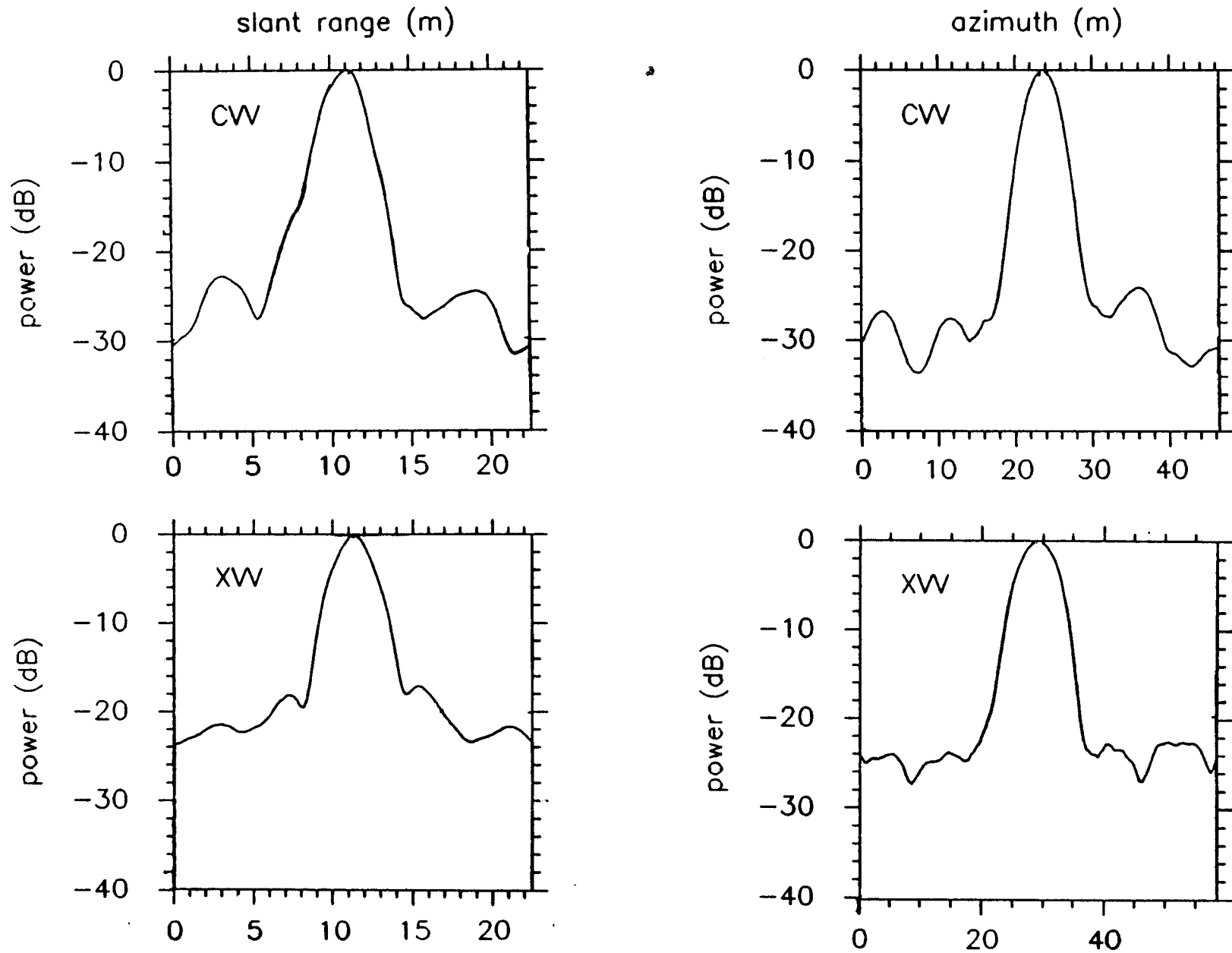


Figure 11. Range and azimuth cuts of 0.9 m trihedral impulse response, from E-SAR C-Band and X-Band VV polarized data

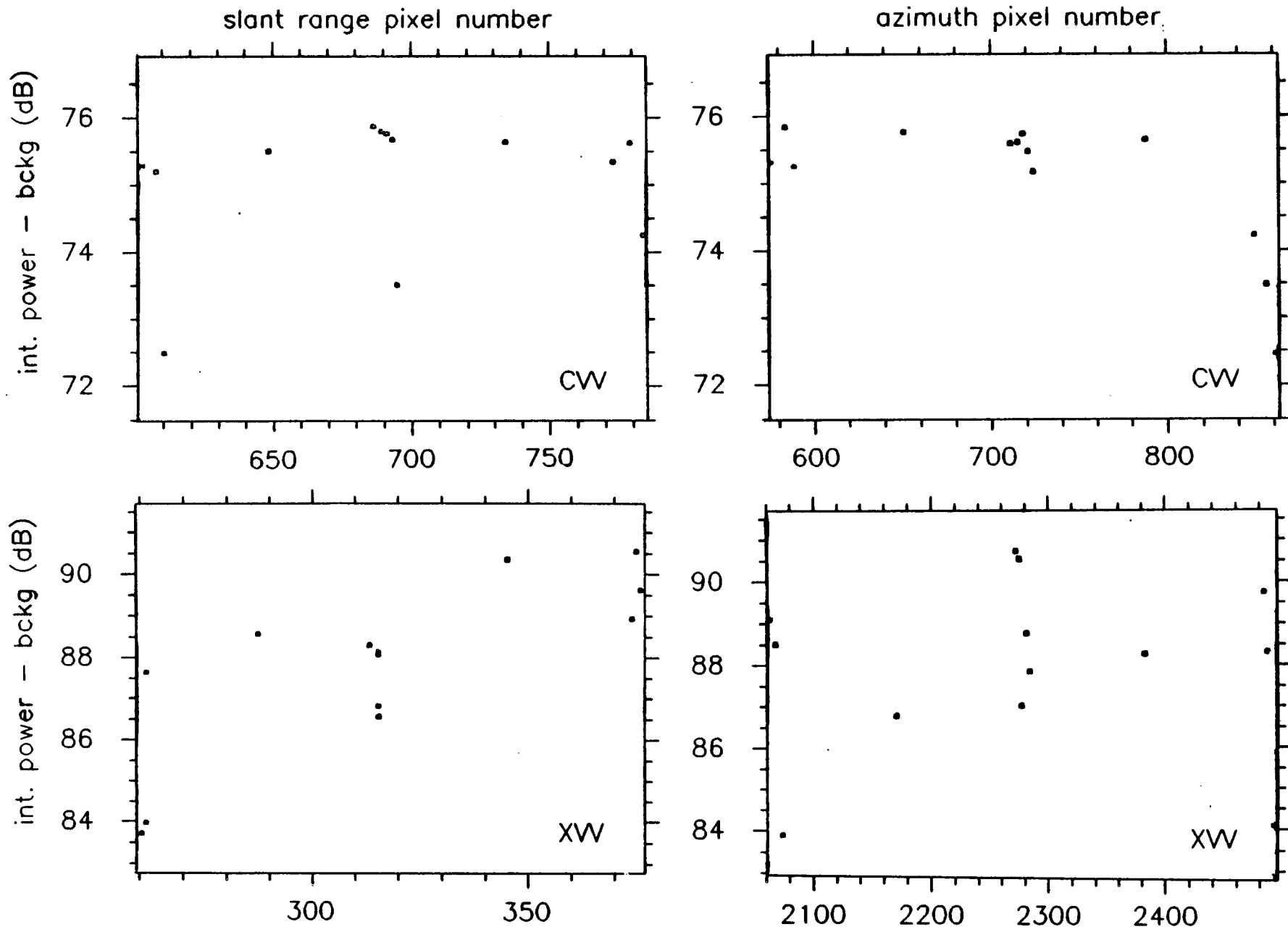


Figure 12. Range and azimuth variations of 0.9 m trihedral responses, from E-SAR C-Band and X-Band images

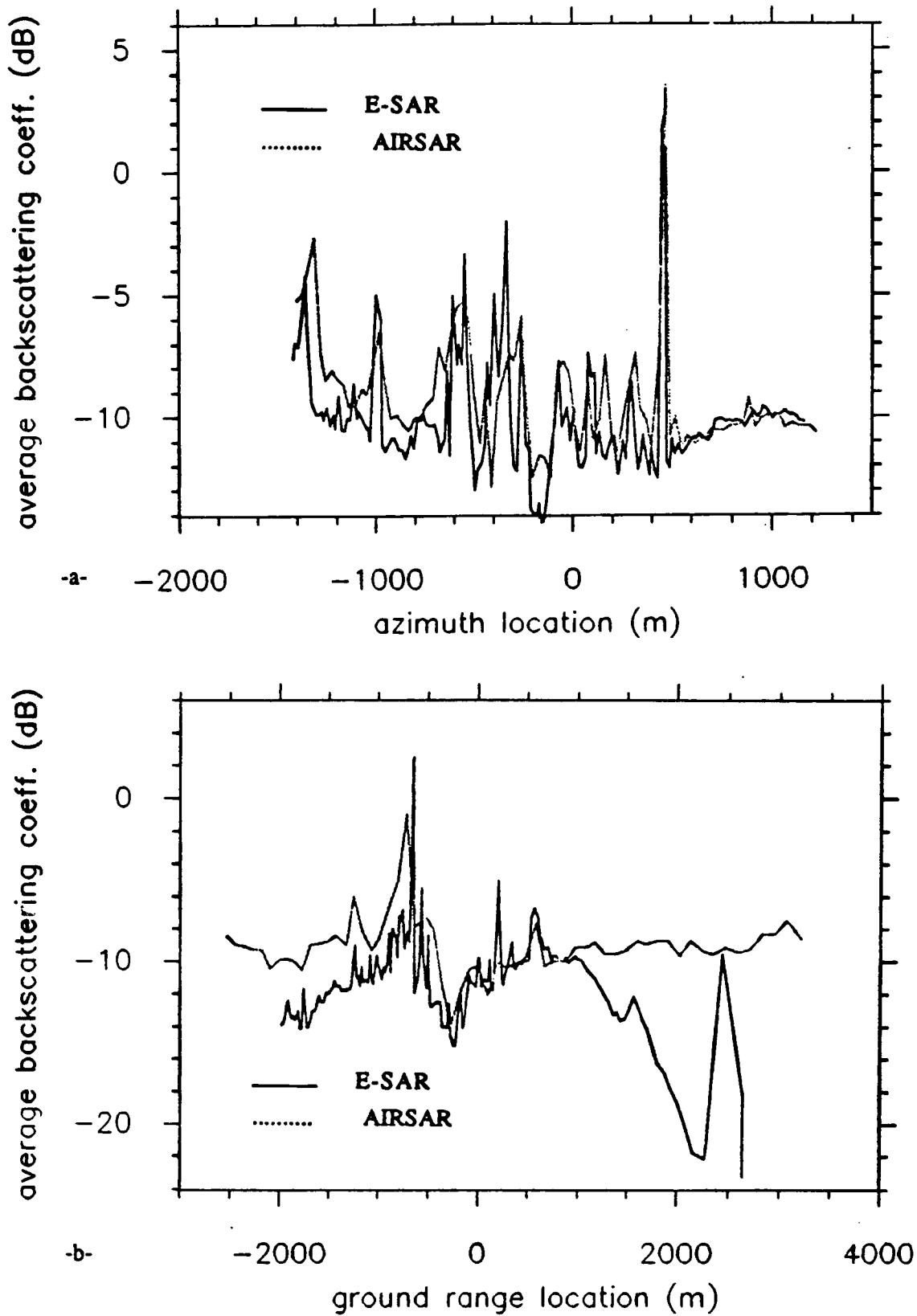


Figure 13. Azimuth and ground range variations of the average backscattering coefficient, from E-SAR and AIRSAR calibrated CVV images

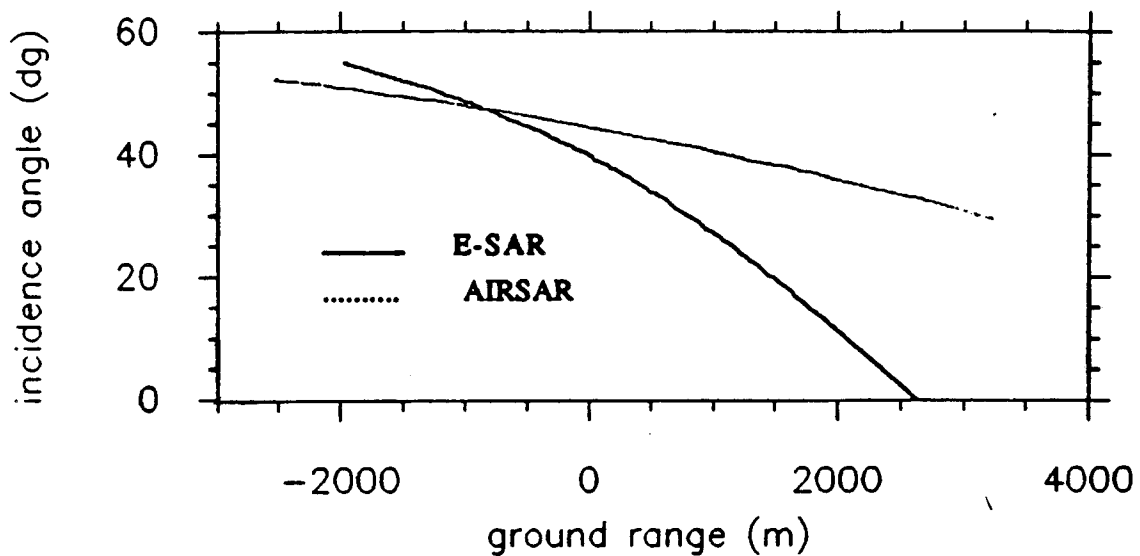


Figure 14. E-SAR and AIRSAR incidence angle variation versus ground range location

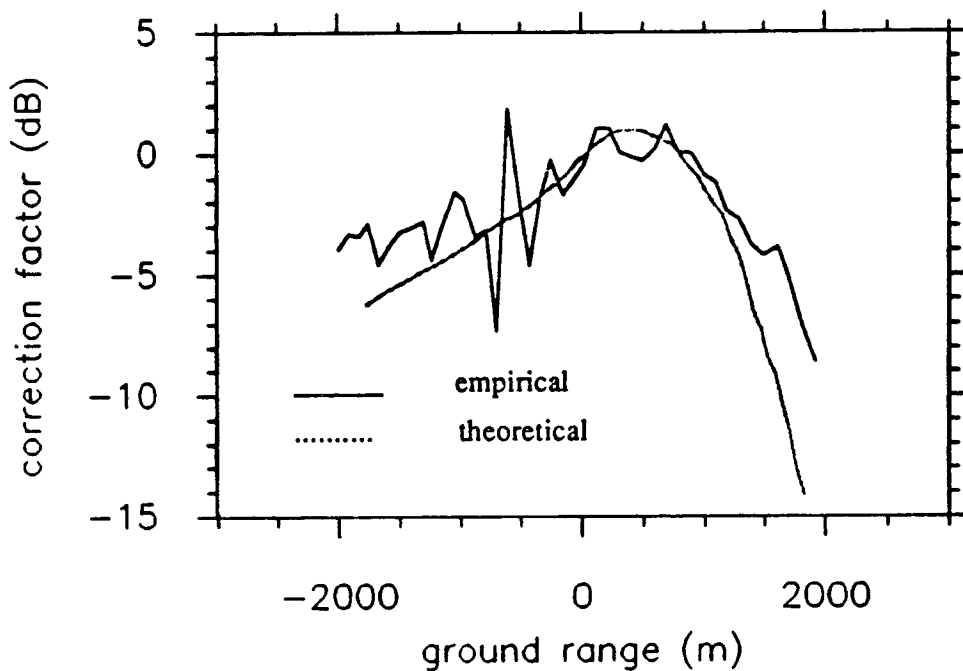


Figure 15. E-SAR C-Band relative calibration in the range direction: theoretical (from antenna pattern data) and empirical (from AIRSAR comparison) curves